Journal of African Earth Sciences 192 (2022) 104570

Contents lists available at ScienceDirect

Journal of African Earth Sciences

journal homepage: www.elsevier.com/locate/jafrearsci

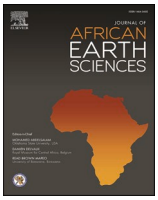

Across and along-strike crustal structure variations of the western Afar margin and adjacent plateau: Insights from receiver functions analysis

Abdulhakim Ahmed [a,b,*], Cecile Doubre [a], Sylvie Leroy [b], Derek Keir [c,d], Carolina Pagli [e], James O.S. Hammond [f], Atalay Ayele [g], Maxime Be de Berc [a], Marc Grunberg [h], Jerome Vergne [a], Romain Pestourie [a], Daniel Mamo [g], Birhanu Kibret [g], Nadaya Cubas [b], Aude Lavayssière [c,i], Marianne Janowski [b], Olivier Lengliné [a], Alessandro La Rosa [e], Emma L. Chambers [c,j], Finnigan Illsley-Kemp [k]

[a] Université de Strasbourg, CNRS, ENGEES, ITES UMR 7063, F-67000 Strasbourg, France
[b] Sorbonne Université, CNRS-INSU, Institut des Sciences de la Terre de Paris, ISTEP, Paris, France
[c] School of Ocean and Earth Science, University of Southampton, Southampton, United Kingdom
[d] Dipartimento di Scienze della Terra, Università degli Studi di Firenze, Florence, Italy
[e] Earth Science Department, University of Pisa, Pisa, Italy
[f] Department of Earth and Planetary Sciences, Birkbeck, University of London, Malet Street, WC1E 7HX, London, UK
[g] Institute of Geophysics, Space Science and Astronomy, Addis Ababa University, Addis Ababa, Ethiopia
[h] Université de Strasbourg, CNRS, EOST UMS 830, F-67000, Strasbourg, France
[i] Institut de Physique du Globe de Paris, Université de Paris, CNRS, F-7500, Paris, France
[j] Dublin Institute for Advanced Studies DIAS, Dublin 2, Ireland
[k] School of Geography, Environment and Earth Sciences, University of Wellington, Wellington, New Zealand

ARTICLE INFO

Keywords:
Africa
Continental margin
Afar margin
Southern red sea rift
Receiver functions
Crustal structure

ABSTRACT

We used teleseismic receiver function analysis to image the crustal structure beneath 24 broadband seismic stations densely deployed along two profiles traversing different structural units across the western Afar margin. Our high-resolution receiver function results image pronounced spatial variations in the crustal structure along the profiles and provide improved insights to understand how strain is partitioned in the crust during rifting. Beneath the western plateau next to northern Afar, the crust is likely felsic-to-intermediate in composition (average Vp/Vs 1.74), with a step like thinning of the crust from an average of 38 km beneath the western plateau to an average of 22 km beneath the marginal graben. Consistently thicker crust is observed beneath the southern profile (central Afar), showing four distinct regions of uniform crustal thickness: 1) an average crustal thickness of 42 km beneath the western plateau; 2) 34 km beneath the foothills area; 3) 28 km beneath the marginal graben and the wide extensional basin and 4) 21 km beneath the central rift axis. We use crustal thickness results to estimate a stretching factor β of 2.2 and 2.7 for central Afar and northern Afar respectively. Our estimated values are lower than $\beta > 3.0$ predicted from plate reconstructions, and we interpret that the variations are best explained by 2–5 km magmatic addition into the crust. The crustal composition beneath the southern profile is more complex with elevated Vp/Vs ratios ranging between 1.79 and 1.85 beneath the western plateau and marginal graben. This is consistent with a greater mafic component and best explained by crust altered by intrusions due to significant pre and syn-rift magmatic activity. Abnormally high Vp/Vs ratios of more than 1.90 are observed beneath the axial rift zone of central Afar, which most likely suggests the localization of partial melt within the crust.

1. Introduction

The Afar Depression lies in northeast Africa where the Red Sea and Gulf of Aden oceanic spreading ridges and the intra-continental East-African Rift meet, forming a rift-rift-rift triple junction between the Nubian, Somalian, and Arabian plates (McKenzie et al., 1972; Courtillot,

* Corresponding author. Université de Strasbourg, CNRS, ENGEES, ITES UMR 7063, F-67000 Strasbourg, France.
E-mail address: hakim.qubati66@gmail.com (A. Ahmed).

https://doi.org/10.1016/j.jafrearsci.2022.104570
Received 19 April 2021; Received in revised form 19 April 2022; Accepted 21 April 2022
Available online 4 May 2022

1982; Tesfaye et al., 2003; Doubre et al., 2017). The Afar Depression is bound by the continental Danakil block to the northeast (Fig. 1), and by the western and south-eastern Ethiopian plateaus, to the west and south-east respectively. The Afar Depression is thought to have formed shortly after the impact of the Afar mantle plume and associated eruption of the bimodal Ethiopia-Yemen Trap Series of basalts and rhyolitic lavas (Baker et al., 1996a; Hofmann et al., 1997; Pik et al., 1998, 1999; Beccaluva et al., 2009; Pik, 2011; Natali et al., 2016; Krans et al., 2018). The extension of the proto-African lithosphere started in the Oligo-Miocene (~29-26 Ma) shortly after the peak in Trap Series volcanism at ~29–31 Ma (Wolfenden et al., 2004, 2005; Stab et al., 2016). In the present-day, several ~50–60 km long, ~15–20 km wide magmatic segments are the locus of extensional deformation with networks of normal faults formed above narrow zones of episodic dike intrusion (Fig. 1b; Wright et al., 2006; Grandin et al., 2009; Smittarello et al., 2016; Barnie et al., 2016; Ebinger et al., 2017). Therefore, the continental margin of the Afar region is a unique location where the transition from the stable continental plateaus to incipient seafloor spreading within the Afar rift axis is subaerially exposed (Barberi and Varet, 1977; Hayward and Ebinger, 1996; Beyene and Abdelsalam, 2005; Medynski et al., 2016).

Continental rifting leading to continental breakup and oceanic spreading encompasses a complex interplay of extensional faulting, thinning of the crust and lithosphere and intrusive-extrusive magmatism (Buck, 2004; Geoffroy, 2005; Lavier and Manatschal, 2006; Cannat et al., 2009; Leroy et al., 2010; Nonn et al., 2019). The estimation of the crustal thickness, Moho depth, crustal composition, stretching/thinning factors (β) and the magmatic additions to the crust is important for understanding the pre-seafloor spreading evolution of rifted continental margins. The Afar crust has been imaged along rift with a seismic refraction survey (Berckhemer et al., 1975; Makris and Ginzburg, 1987), revealing that the crustal thickness is about 23–26 km at the south and thins to ~14 km in the north. The crustal thickness variations and internal seismic structure of the Afar margin have to date been investigated using receiver function studies from seismic networks with sparse station spacing (~40-km) (Dugda et al., 2005; Dugda and Nyblade, 2006; Hammond et al., 2011; Kibret et al., 2019; Wang et al., 2021). High stretching value of $\beta > 3.0$ predicted from plate reconstructions for the Afar Depression (e.g. Eagles et al., 2002), is higher than $\beta \approx 2.7$ and $\beta \approx 2.0$ estimated for central and southern Afar from cross section balancing (Stab et al., 2016) and gravity data inversions (Tiberi et al., 2005), respectively. By using the seismic structure beneath Addis-Ababa and Mile from the Berckhemer et al. (1975) refraction profile, Mohr (1983) suggested décollement style deformation to explain the differential upper/lower crustal layers extension. Similarly, using observations from previous receiver function studies and seismic profiles, Stab et al. (2016) favored a flat detachment at mid-crustal level to interpret the difference in the upper/lower crustal layers extension in central Afar. Reed et al. (2014) noticed a diffuse and localized current extensional strain in the lower and upper crustal layers, respectively, beneath southern Afar. They argued for a high degree of decoupling between the brittle upper crust and ductile lower crust. In northern Afar beneath the Danakil depression the crustal extension is accommodated by faulting in the upper crust and coupled ductile extension of the lower crust and mantle lithosphere (Bastow et al., 2018). However, none of the previous studies offer a sufficiently good image of the crustal structure across the margin to unravel the extensional history and any along-margin variations in the role of tectonics and magmatism during the continental breakup.

A detailed image of the deformation will help to constrain the structure and evolution of the margin prior and coeval with the continental rifting and answer some of the remaining questions: Does the stretching and the thinning of the continental crust occur over a narrow or broad region? Is the rifting smooth or stepped? Is the existent of the differential extension between the crustal layers from the early stages or only during the late stages of the rift evolution? What are the interactions between mechanical stretching and thinning of the crust, and magma intrusions (e.g. Keir et al., 2013)?

In order to resolve the high-resolution crustal structure of the western margin of the Afar Depression for the first time, we analyze data from 24 temporary broadband stations distributed along two densely sampled profiles going from the western plateau to central and northern Afar. We use P-to-S receiver functions (Phinney, 1964; Burdick and Langston, 1977; Langston, 1977; Ammon, 1991) to image the crust-mantle transition and intracrustal discontinuities as well as to infer crustal properties from Vp/Vs values obtained using the H-k stacking

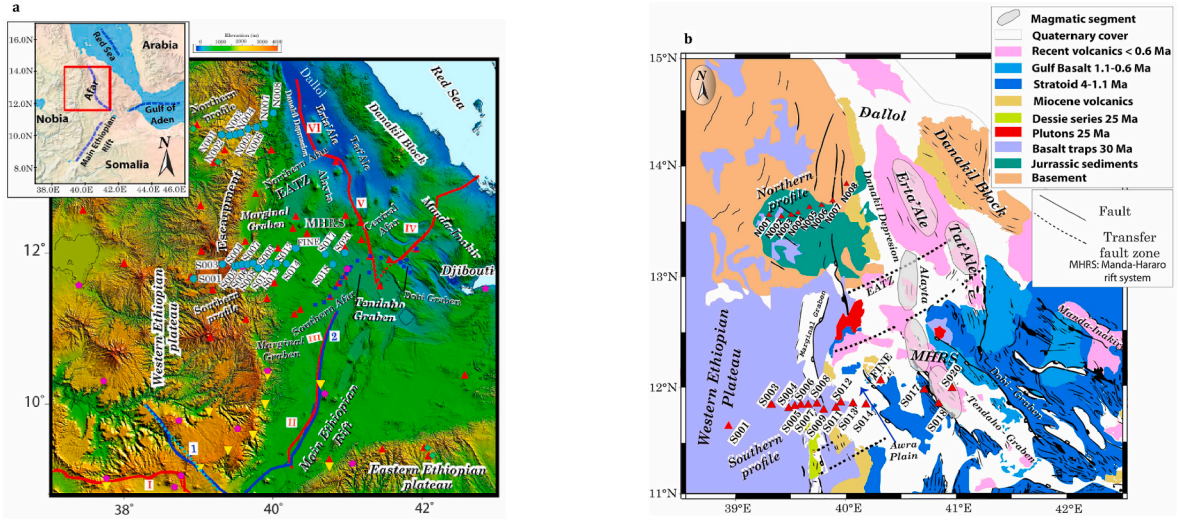

Fig. 1. a) Topographical map of Afar and surrounding areas show the locations of the seismic stations used for the current study and the published crustal structure and composition works. Light blue circles represent the distribution of the broadband stations along two profiles used in this study. Previous receiver function studies (red triangles, Hammond et al., 2011; inverted yellow triangles, Stuart et al., 2006; magenta pentagon, Dugda et al., 2005; blue squares, Rooney et al., 2018; green diamonds, Ogden et al., 2019; dotted cyan line, Cornwell et al., 2010). Red lines (I-VI) indicate the location of the active seismic profiles of Berckhemer et al. (1975) and Makris and Ginzburg (1987). Blue lines (1 and 2) show location of the active seismic profile of Maguire et al. (2006). MHRS: Manda Harraro Rift Segment. Inset at the upper right left corner is a regional map show the location of the study area. b) geological map of the Afar Depression and surrounding highlands modified from Stab et al. (2016) and Le Gall et al. (2018). (For interpretation of the references to colour in this figure legend, the reader is referred to the Web version of this article.)

method (Zhu and Kanamori, 2000). This allows us to understand the spatial relationships between plate stretching, thinning and magma intrusion during continental breakup.

The comparison of the crustal structure along the two profiles allows us to estimate the longitudinal variations of the rifting along the margin and the respective role of tectonics and magmatism. Assuming that the crustal thickness beneath the western plateau at the location of each profile is representative for the crustal thickness just before the onset of the crustal extension (postdate the flood basalts event), we use the crustal thicknesses of our profiles to calculate the stretching factor across the rift margin. We compare our observed crustal thicknesses and stretching factors to those predicted from plate kinematic models to estimate the melt added to the crust.

2. Background

2.1. Geological and tectonic settings

Rifting along the Gulf of Aden initiated ~34 Ma ago (Leroy et al., 2012) followed by the emplacement of voluminous Ethiopia-Yemen Trap Series on the Ethiopian and Yemeni plateaus ~31-29 Ma ago (Baker et al., 1996a; Hofmann et al., 1997; Ukstins et al., 2002; Rooney, 2017). On the Ethiopian plateaus, they erupted and covered a thick series of Mesozoic sedimentary rocks (Bosworth et al., 2005; Beyene and Abdelsalam, 2005) currently outcropping on the western plateau, overlying the Neoproterozoic crystalline basement rocks (e.g. Alemu et al., 2018; Le Gall et al., 2018, Fig. 1b). They also likely covered parts of the region that would become the Afar Depression.

The rifting within the Afar is thought to have initiated at ~29-26 Ma, postdating the main flood basalt event (ca. 31-29 Ma; Rooney, 2017). Geological studies from the central and southern parts of the western margin of Afar propose three main stages of strain migration from the border faults to the current magmatic segments (Wolfenden et al., 2005; Rooney et al., 2018; Stab et al., 2016). In stage 1, starting just after the flood basalt deposits of 29 to 26 Ma, narrow half-grabens initiate the rift, coeval with the emplacement of rhyolites in these basins. Stage 2 (16-7 Ma) corresponds to the eastward migration of extensional deformation towards the rift axis, accompanied by fissural basaltic volcanism. Finally, Stage 3 (<7 Ma) includes a further eastward jump in the locus of extension and increase in localized magma intrusion and voluminous basalts. Stage 3 is responsible for eruption of a ~1.5-km-thick Stratoid Series lava pile of mostly basalts emplaced at 4.0–1.1 Ma that now covers 70% of Afar (Varet, 1975; Stab et al., 2016, Fig. 1b). After 1.1 Ma, the deformation and magmatism became localized within discrete seismically and volcanically active magmatic segments characterized by intense diking and volcanism (e.g. Barberi et al., 1972; Abdallah et al., 1979; Hayward and Ebinger, 1996; Manighetti et al., 1998; Wright et al., 2006; Grandin et al., 2009).

Extensional basins in southern and central Afar are filled with Pliocene–Recent lacustrine and fluviatile sedimentary rocks interbedded with basaltic and felsic lava flows (Tesfaye et al., 2003). In northern Afar, the Danakil basin is known to include at least 1 km of Holocene-Recent evaporites (e.g. Bastow et al., 2018; Le Gall et al., 2018). However, the sedimentary basin likely extends to 3–5 km depth with Pliocene-Pleistocene-Recent age evaporites and basalt flows (Bastow and Keir, 2011; Keir et al., 2013).

The western Afar margin preserves the rift morphology since the onset of the flood basalt till the initiation of the seafloor spreading (Tesfaye et al., 2003; Wolfenden et al., 2005; Keir et al., 2013; Ebinger et al., 2017; Rooney et al., 2018). This margin is characterized by stratigraphic and structural changes from the south toward the north (e.g. Keir et al., 2013). For example, south of latitude 13°N, the transition from the western plateau, covered here by a thick sequence of Trap series, to the extended crust in the Afar Depression corresponds to a zone of antithetic faults forming a wide zone of marginal basins (Wolfenden et al., 2004, 2005; Stab et al., 2016). North of latitude 13°N, where the Trap series does not outcrop on the western plateau, the margin is characterized by normal faults forming a narrow zone of marginal grabens (Justin-Visentin and Zanettin, 1974; Kieffer et al., 2004; Wolfenden et al., 2005; Rooney et al., 2018; Le Gall et al., 2018). The seismic activity is more intense in this area with several events of magnitude greater than 5.0 (Ayele et al., 2007; Illsley-Kemp et al., 2018). These changes along the Afar margin are spatially associated with a northward thinning of the crust within the rift, and surface area of Holocene volcanism (Barberi and Varet, 1977; Berckhemer et al., 1975; Makris and Ginzburg, 1987; Hammond et al., 2011; Bastow and Keir, 2011; Rooney, 2020).

2.2. Previous constraints on crustal structure

Previous geophysical studies have contributed significantly to our knowledge of the crustal structure of our study area (Fig. 1a). Estimates of the crustal thickness and crustal composition beneath Afar and surrounding plateaus have been made using controlled source seismic profiling (e.g Makris and Ginzburg, 1987; Mackenzie et al., 2005; Maguire et al., 2006), inversion of gravity data (e.g. Makris et al., 1991; Tiberi et al., 2005) and magnetotelluric imaging (e.g. Desissa et al., 2013; Didana et al., 2014; Johnson et al., 2016). Also using passive seismic techniques, such as P-to-S (e.g. Dugda et al., 2005; Hammond et al., 2011; Rooney et al., 2018; Ogden et al., 2019; Wang et al., 2021), S-to-P receiver functions (e.g. Lavayssiere et al., 2018), surface wave tomography (e.g. Gallacher et al., 2016) and ambient noise tomography (e.g. Korostelev et al., 2015; Chambers et al., 2019).

Makris and Ginzburg (1987) used the data from an along strike seismic refraction profiles (Fig. 1a) to propose a four-layer crustal structure within the Afar Depression underlain by an anomalous upper mantle (P_n velocity of 7.4–7.5 kms^{-1}). This model consists of a 3–5 km sedimentary cover (a P-wave velocity, Vp of 3.35–3.95 kms^{-1}), that overlies a basaltic layer (Vp = 4.5 kms^{-1}) on a 2–6 km abnormally thin upper crust (Vp of 6.1–6.2 kms^{-1}) and a lower crust (Vp of 6.7–7.0 kms^{-1}). This study shows that the crust thins from 26 km in the south and central Afar to 14 km in the north. Crustal thickness inferred from gravity data (Makris et al., 1991; Tiberi et al., 2005) shows thin crust beneath the Afar rift (14–23 km) and thick (~40 km) continental crust beneath the western plateau that is partly intruded with high-density material.

Previous P-to-S receiver function studies (Dugda et al., 2005; Stuart et al., 2006; Hammond et al., 2011; Rooney et al., 2018; Kibret et al., 2019; Wang et al., 2021, Fig. 1a) and a joint inversion of Rayleigh wave velocities and receiver functions (Dugda et al., 2007) confirm these variations, showing ~20–26 km thick crust beneath the Afar Depression and rapidly thinning to ~16 km beneath the Danakil Depression of northern Afar (e.g. Hammond et al., 2011). The estimated crustal thickness beneath the western and south-eastern plateaus ranges from 36 to 45 km (Dugda et al., 2005; Stuart et al., 2006; Cornwell et al., 2010; Hammond et al., 2011; Kibret et al., 2019; Wang et al., 2021). These studies also show a normal to elevated Vp/Vs ratio for the plateaus and reaching very high values (Vp/Vs > 2.0) near the magmatic segments where the crustal thickness is less than 26 km (e.g. Hammond et al., 2011; Wang et al., 2021). A seismic anisotropy study (Hammond, 2014) shows that the melt beneath the Afar Depression is stored in interconnected stacked sills within the lower crust consistent with high Vp/Vs ratios of more than 1.95 obtained by receiver function analysis, an interpretation supported by slow lower crustal S-wave velocities imaged using ambient noise tomography (e.g. Chambers et al., 2019; Korostelev et al., 2015). In addition, S-to-P receiver functions identify a velocity decrease with depth at 65–75 km beneath the western plateau interpreted as the lithosphere-asthenosphere boundary (LAB; Rychert et al., 2012; Lavayssiere et al., 2018). The LAB is not imaged below Afar and interpreted as evidence of melt percolation into the mantle lithosphere (Lavayssiere et al., 2018).

However, the seismic stations used in the previous studies (Dugda

et al., 2005; Stuart et al., 2006; Hammond et al., 2011; Lavayssiere et al., 2018; Chambers et al., 2019; Wang et al., 2021) were deployed at a spacing of several tens of kilometers and those used by Reed et al. (2014) were located along a profile across the south-eastern part of central Afar. Thus, these studies are limited in providing high-resolution images of the crustal structure from the continental stable plateaus to the active rift axes.

3. Data and methodology

3.1. Data

From May 2017 to September 2018, a network that included 9 SEIS-UK broadband seismic stations (7 Guralp CMG-3ESPD-60s and 2 CMG-40T-30s with Guralp CMG-DCM datalogger) and 20 French Sismob-RESIF broadband seismic stations (Guralp CMG-40T-30s with Nanometrics Taurus digitizer) was deployed along two SW-NE oriented profiles, more or less perpendicular to the large fault scarps forming the western Afar margin and the main axis of the Afar rift (Fig. 1). This network has been configured to image the crustal structure across the transition from the western plateau to the currently active rifts of the northern and central parts of Afar (Fig. 1). For northern Afar we used 8 stations (N001 to N008) deployed along an 86 km-long profile spaced by an average distance of 11 km (Keir, 2017, Fig. 1). For central Afar we used 15 stations (S001, S003 to S009, S011 to S014, S017, S018 and S020) deployed along a ~225 km-long profile spaced at ~20 km at the ends and ~10 km in the middle of the profile (Doubre et al., 2021, Fig. 1). For improved continuity of the southern profile, we added data from FINE station installed from March 2007 to November 2009 (Ebinger, 2007). All stations recorded continuous data with a sampling rate of 100 Hz except FINE, which recorded continuous data at 50 Hz.

For the receiver function analysis, the IRIS earthquake catalog was searched for events with magnitude, Mb $\geq$ 5.5, occurring within an epicentral distance range of 30°–95° from the center of the network. To increase the azimuthal coverage, regional events between 20° and 30° were also included (e.g. Park and Levin, 2001; Salmon et al., 2011, Fig. 2a), with a specific treatment detailed in section 3.2.1. In total, waveforms from 186 earthquakes including 11 regional events were selected.

The data were manually inspected and rated based on the signal-to-noise ratio (S/N; the ratio between the amplitude of the signal at P-arrival time to the maximum amplitude of the 5 s pre-arrival noise window), where only low-noise traces (S/N > 4) with a clear P wave arrival recorded at each station, were kept for further analysis. This process resulted in the selection of ~126 earthquakes (including 11 regional events) for receiver function construction and processing (Fig. 2a). After removing the mean and the first-order trends from the selected waveforms, the data were filtered using a zero-phase Butterworth bandpass filter with corner frequencies of 0.05–1.5 Hz (e.g. Zhu L., 2000; Nair et al., 2006). Waveforms from two stations located at the edge of the plateau and characterized by noisy data are bandpass filtered (0.02–0.8 Hz) to remove the high frequency noise above 1 Hz. Then the traces were windowed 5 s before and 35 s after the theoretical P arrival time and the horizontal seismograms were rotated into a great-circle path from the ZNE coordinate system to the ZRT coordinate system.

3.2. Methods

3.2.1. P-to-S receiver functions

The receiver function technique is widely used to image seismic discontinuities beneath a seismic station by deconvolving the vertical component from the radial and/or transverse components. This aims to remove the instrument response, the propagation path and the source mechanism effects from a broadband teleseismic record (Langston, 1977, 1979). We used the iterative time domain deconvolution technique of Ligorria and Ammon (1999) to compute the receiver functions

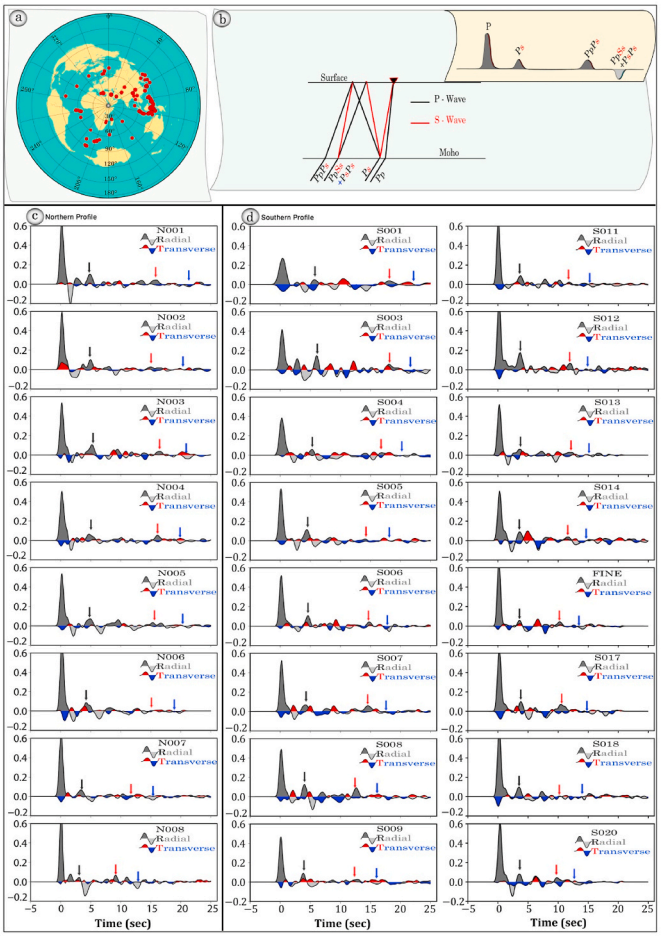

Fig. 2. a) Map showing the distribution of the ~126 teleseismic events selected and used for receiver functions analysis in this study centered at the network location, b) sketch illustrating the path of the converted phases. Stacked radial (dark/grey fill colour) and transverse (red/blue fill colour) receiver functions for the 23 seismic stations along two profiles; c) the northern profile - Danakil Depression, and d) the southern profile at the latitude of the central Afar. The black, red and blue arrows represent the onset of the Pms converted phase and its multiples PpPs and PpSs-PsPs respectively. (For interpretation of the references to colour in this figure legend, the reader is referred to the Web version of this article.)

with 200 iterations. We used a Gaussian width factor of 2.5 in the deconvolution of the vertical trace to predict the radial one (Ligorria and Ammon, 1999), except for two noisy stations located at the edge of the plateau for which we used a Gaussian width factor of 2.0 to excluded high frequency noise above ~1 Hz. The percentage of recovery was evaluated from the rms misfit between the original radial waveform and the radial receiver function convolved with the vertical component. If the final deconvolution reproduces less than 80% of the signal, then the event is discarded from further analysis. From this, together with a visual inspection for coherence and stability, the number of receiver functions included in the final analysis varied between 15 and 72 per station (Table 1), depending on the background noise and the state of health of the station.

Extra care is required for using regional events in the receiver function analysis. They are susceptible to complex P-wave arrivals due to upper mantle triplications (e.g., Chu et al., 2012). To check for any artifacts due to triplicated phases, we only kept the events that will not change the H and/or Vp/Vs beyond the error limits determined from the teleseismic events alone. For example, station S005 had a maximum number of 10 regional events, whereas for most of the other stations they are less than six. Fig. S1b and Fig. S1c show the RFs and H-k plots

Table 1
Crustal thickness (H), Vp/Vs ratio for the seismic stations and associated uncertainty estimates deduced from the bootstrap analysis.

Station	Latitude	Longitude	Elevation (m)	H (km)	Error H (km)	Vp/Vs	Error Vp/Vs	Number of RF
N001	39.3077	13.5545	2148	37.2	2.0	1.73	0.04	45
N002	39.4162	13.5453	2000	38.8	2.1	1.73	0.01	24
N003	39.5007	13.5580	2080	37.6	0.5	1.79	0.02	47
N004	39.5653	13.5775	2265	37.6	0.3	1.73	0.01	60
N005	39.6677	13.6334	2270	38.6	1.6	1.73	0.04	36
N006	39.7805	13.6509	2383	37.0	7.0	1.70	0.10	50
N007	39.8938	13.6922	970	24.2	1.4	1.79	0.02	29
N008	40.0066	13.8406	692	19.6	1.0	1.93	0.04	35
S001	38.9328	11.6591	2904	42.8	1.7	1.79	0.01	23
S003	39.3211	11.8511	3446	40.8	0.8	1.89	0.01	57
S004	39.4903	11.8274	2372	37.2	4.0	1.83	0.06	15
S005	39.5291	11.8387	1931	34.2	1.9	1.76	0.03	55
S006	39.5874	11.8472	2057	34.0	0.4	1.76	0.02	58
S007	39.6583	11.8478	1601	33.8	1.4	1.72	0.01	56
S008	39.7348	11.8621	1491	28.4	0.3	1.83	0.01	47
S009	39.7995	11.8001	1486	28.6	0.5	1.79	0.01	51
S011	39.9164	11.8203	1075	27.6	1.4	1.79	0.01	58
S012	39.9581	11.8717	1007	28.0	1.1	1.77	0.01	17
S013	40.0506	11.8574	914	27.8	1.4	1.79	0.01	26
S014	40.1831	11.8584	827	20.4	1.3	1.94	0.08	26
FINE	40.3100	12.0600	782	21.4	0.4	1.99	0.02	72
S017	40.7044	11.9856	613	23.2	1.3	1.95	0.01	59
S018	40.8044	11.8521	441	21.2	1.0	1.91	0.01	15
S020	40.9667	12.0019	355	19.6	0.8	2.04	0.02	50

from station S005 with and without the regional events included, respectively. The estimated crustal thickness and Vp/Vs are approximately the same. Similarly, Fig. S1d shows binned and stacked receiver functions in epicentral distance of 10° for three stations that have six or more regional events. It is clear that the results from regional events (20°–30°) are comparable to the results from teleseismic events (30°–95°) for each station.

3.2.2. H–κ Stacking

To determine the average crustal properties, we analyzed receiver functions for each station using the H-κ domain stacking technique of Zhu and Kanamori (2000). This method enables the determination of Moho depth (H) and the velocity ratio of crustal P and S phases (Vp/Vs, or κ) by considering the crust as a homogeneous, horizontal, isotropic layer over a half-space. The inherited trade-off in the receiver function analysis between the crustal thickness (H) and the average crustal velocity properties can be partially resolved using the H-κ stacking algorithm (Ammon et al., 1990), if a good assumption can be made about the average P-wave velocity from nearby refraction profiles (e.g. Makris and Ginzburg, 1987). With this information, we sum amplitudes of the receiver functions at predicted arrival times for the Moho P-to-S conversion phase Pms and its multiple converted phases PpPs and PpSs + PsPs (Fig. 2b), using different weights and a range of H and Vp/Vs values.

The stacking amplitude in the H-k domain is given by:

$$s(H,\ k) = \sum_{m=1}^{n} w_1 r_m(t_{p_s}) + w_2 r_m(t_{p_p p_s}) - w_3 r_m(t_{p_p S_s + p_s P_s}) \quad (1)$$

where n is the number of radial receiver functions at each station, W_j is a weighting factor that represents the contribution of the direct conversion from the Moho and its multiples according to signal-to-noise ratio ($W_1 + W_2 + W_3 = 1$) and $r_m(t)$ is the amplitude of the point on the receiver function at predicted arrival time t (after the first P arrival) of the associated seismic phase corresponding to the crustal thickness H and Vp/Vs. The stacking amplitude reaches its maximum as the three phases stack coherently, and represents the best estimate for both H and Vp/Vs (κ) beneath the station. Globally, we follow the same weighting factor scheme $W_1 = 0.7$, $W_2 = 0.2$ and $W_3 = 0.1$ of Zhu and Kanamori (2000) that balances the contribution of each phase proportional to low signal-to-noise ratio of multiples. We modified the weighting factors in a few cases, by increasing those for multiples when the Moho conversion phase amplitude is low ($W_1 = 0.5$, $W_2 = 0.3$ and $W_3 = 0.2$: N008; Figs. 2c and 3a) or when high-amplitude intra-crustal interface conversion phases obscured the Moho Pms conversion ($W_1 = 0.4$, $W_2 = 0.3$ and $W_3 = 0.3$: N002; Fig. 2c), or by decreasing them when the multiples are less clearly identifiable ($W_1 = 0.8$, $W_2 = 0.1$ and $W_3 = 0.1$: S018: Fig. 2d).

In this study, we allowed the crustal thickness H and Vp/Vs ratio to vary within reasonable extremes determined with constraints from previous measurements (e.g. Dugda et al., 2005; Hammond et al., 2011; Rooney et al., 2018; Ogden et al., 2019). For all the stations, the searching range for H is 10–50 km, whilst the Vp/Vs search range for the stations located on the plateau and within the Afar marginal area was restricted to 1.6–1.95. The search range of the Vp/Vs ratio for the stations located within and near the rift axis, was restricted between 1.6 and 2.20. We used a search step of 0.1 km for H and 0.01 for Vp/Vs.

The Vp/Vs ratio derived from the H-κ stacking method is related to the elastic parameter Poisson's ratio (σ) through the simple relationship $\sigma = 0.5(1\text{-}\{1/[(V_P/V_S)^2 - 1]\})$ (Zandt and Ammon, 1995; Ligorria, 2000), and is typically used to provide important constraints regarding the bulk crustal composition (e.g. Christensen, 1996; Chevrot and van der Hilst, 2000). Poisson's ratio variations mainly depend on mineralogical composition of the crust (felsic, mafic) and/or the presence of fluids rather than on pressure or temperature conditions (Christensen, 1996; Watanabe, 1993).

3.2.3. Results stability and uncertainty estimates

Three important factors control the stability of the H-κ inversion results using the receiver function method: 1) the average crustal P-wave velocity used to do the inversion; 2) the back-azimuth coherency of the Moho converted phase Pms and multiples PpPs and PpSs + PsPs and 3) the level of noise in the receiver function waveform data.

Average crustal P-wave velocity (Vp) used in previous receiver function studies in Ethiopia shows a large range of values (4.6 kms^{-1} - 6.5 kms^{-1}). For example, Dugda et al. (2005) tested three different average crustal velocity values Vp = 6.3 kms^{-1}, Vp = 6.5 kms^{-1} and Vp = 6.8 kms^{-1} and chose the one that gave the best results for H and Vp/Vs ratio. Stuart et al. (2006) used three different Vp values constrained from the EAGLE controlled-source profile of 6.1 kms^{-1}, 6.15 kms^{-1} and 6.25 kms^{-1} for the southern, central Ethiopian rifts, and adjacent

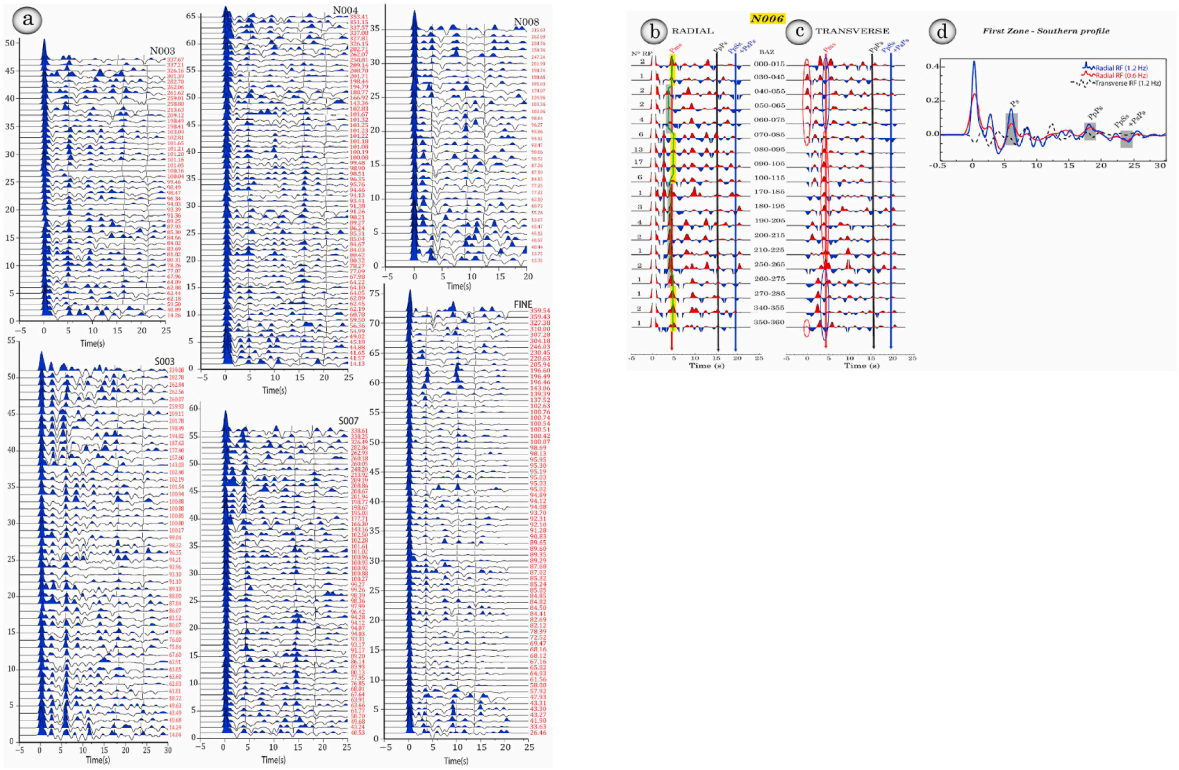

Fig. 3. a) Individual receiver functions for six stations. The receiver functions are organized by increasing backazimuth (value in red). The light vertical lines indicate arrival times for conversion phases (Pms and multiples) from the Moho for the maximum stacking amplitude;; b) Ps radial RFs at the N006 seismic station for good quality data within an epicentral range 30°–95°, stacked in backazimuth into bins of 15° and with an overlap of 5°. The numbers of RFs in each stack are indicated above each trace to the left and the backazimuth ranges to the right; c) Ps transverse RFs at the N006 seismic station stacked with the same epicentral distance, backazimuth ranges and number of RFs in each stack as in b; d) Stacked Ps radial RFs with a maximum frequency of 0.6 Hz (red line) and 1.2 Hz (blue line) at the S003 seismic station located at the eastern edge of the western plateau southern profile (central Afar). The stacked transverse RFs with a maximum frequency of 1.2 Hz is represented by a dashed black line. (For interpretation of the references to colour in this figure legend, the reader is referred to the Web version of this article.)

plateaus respectively. Hammond et al. (2011) used values of 6.15 kms^{-1} and 6.25 kms^{-1} for the stations in Afar and on the Ethiopian plateaus again based on nearby refraction profiles (Makris and Ginzburg, 1987). Finally, the average crustal velocity used by Reed et al. (2014) range from 4.8 kms^{-1} to 5.9 kms^{-1} based on the comparison of the stacking results obtained using different initial Vp values ranging from 4.5 kms^{-1} to 7.0 kms^{-1} and theoretical Vp versus κ curve. The variation in P-wave velocities used is evidence of how variable the crustal structure is across Afar and the surrounding areas. We use P-wave velocities from the controlled source profiles closest to our profiles, as do previous studies. Due to this, it is worth noting that the uncertainties of 0.5 km/s from the range of velocities seen across all RF studies would equate to an error in crustal thickness of ~±3.0 km and ~±0.05 in Vp/Vs.

In this study, we used Vp = 6.3 kms^{-1} for the stations located on the western plateau and 6.0 kms^{-1} for the stations located within the Afar rift based on the controlled-source experiments (Berckhemer et al., 1975; Makris et al., 1975; Makris and Ginzburg, 1987; Mackenzie et al., 2005; Maguire et al., 2006), and the average crustal velocity constraints from the previous receiver function studies (Dugda et al., 2005; Stuart et al., 2006; Hammond et al., 2011; Rooney et al., 2018).

To estimate the standard deviation for both crustal thickness H and Vp/Vs, we employ the bootstrap resampling technique (Efron and Tibshirani, 1986). While we present bootstrap errors in this study to show the stability of our solutions and to be consistent with past studies, these errors present more realistic values when considering variations in crustal structure across the array. The bootstrap analysis was done by repeating the stacking procedure 200 times with random data subsets that are resampled versions of the original data set for each station. The 2σ for each station is shown by error bars in the depth sections and supporting information. The same technique was applied to estimate the errors introduced to the results from the assumed average crustal P-wave velocity used to determine the bulk crustal parameters (H and Vp/Vs; Tiberi et al., 2007). We recalculate H and Vp/Vs values using different average crustal Vp in the range 5.8–6.8 kms^{-1} to test the errors introduced by assuming average crustal Vp (Fig. S5). The results are illustrated in Figs. S5a and S5b as standard deviations. We also, extracted the bootstrap results for two stations of the northern profile and three stations of the southern profile. The obtained results are shown in Figs. S5c and S5d. As suggested by several authors (e.g. Mohsen et al., 2005; Nair et al., 2006; Ogden et al., 2019), for a crustal thickness of less than 50 km, a Vp variation of 0.1 kms^{-1} will affect the Moho depth by a value less than 1 km.

3.2.4. *Receiver function depth migration*

The common-conversion point (CCP) technique is a robust method to transfer the receiver functions from the time-domain to the space-domain (e.g. Kind et al., 2002) and image lateral variations of the subsurface discontinuities along a profile. In this study, we perform a common conversion point (CCP) stacking using the Zhu (2000) technique, which is based on the back projection of the amplitude vector of the receiver functions along the ray paths using a given 1-D velocity model. The 3-D space beneath the profile is binned and the amplitudes of all the radial receiver functions with rays passing through each bin are averaged to get the amplitude for that bin. To create our depth migrated cross-sections along both the northern and southern profiles, we use a 1-D Vp model based on the nearby refraction profiles (Berckhemer et al., 1975; Makris and Ginzburg, 1987; Mackenzie et al., 2005; Maguire et al., 2006) and the IASP91 velocity model (Kennett and Engdahl, 1991). The Vs model at each station location is deduced from the Vp/Vs results of the current study, constrained by the previous RF studies

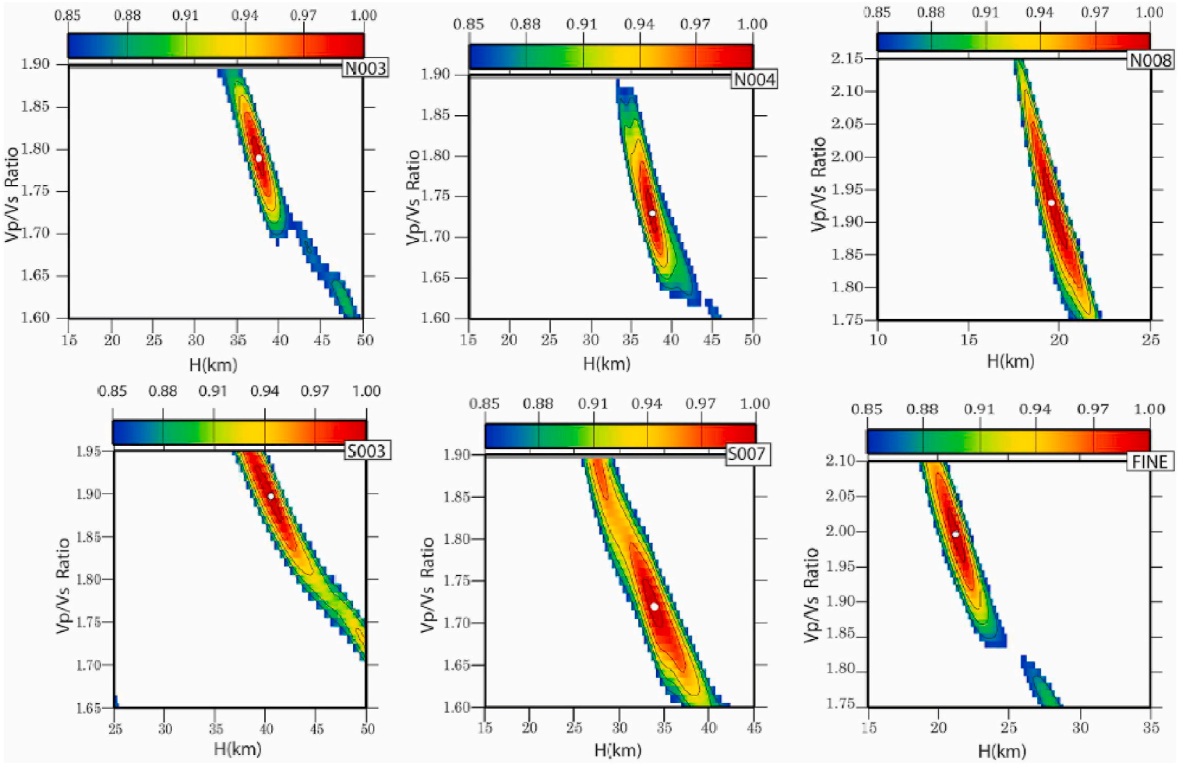

Fig. 4. Thickness (H) versus Vp/Vs ratio diagrams from the H-k stacking method for the 6 stations presented in Fig. 4. The white point indicates the maximum stacking corresponds to the value indicated in Table 1. The scale bar is normalized amplitude of stacking function.

(Stuart et al., 2006; Hammond et al., 2011; Rooney et al., 2018) and Vs models of Chambers et al. (2019). Therefore, the velocity model varies along both profiles (supporting information) and is constrained to maintain the average crustal velocity Vp comparable to that used for H and Vp/Vs calculations. To optimize for the resolution, the CCP depth images are obtained with a bin width of 10 km (equivalent to the estimated width of the first Fresnel zone for an interface at 30 km depth, assuming a signal frequency of 1.2 Hz and S-wave velocity of 3.4 kms^{-1}; e.g. Salmon et al., 2011). The separation between the centers of the bins is set to 2 km to preserve the spatial resolution and the vertical bin width is set to 0.5 km less than the expected vertical resolution equivalent to the half of the minimum wavelength.

4. Results

Most of the stations show a strong and easily identifiable Pms Moho conversion phase on individual and stacked receiver functions (Figs. 2, 3, S1 and S2). The corresponding multiple PpPs, is also identifiable in most cases, but not as consistently visible as Pms, while the latter arrival multiples PpSs + PsPs are often ambiguous and only clearly observed at a few stations. The Moho conversion phase and/or its multiples may be disturbed by reverberations from near surface, low velocity sediment layers and intracrustal and/or upper mantle interfaces at some stations (Figs. 3 and S1). In this study, we present the results ordered and grouped depending on them being on the northern or southern profiles (Fig. 1) and in light of different geological and tectonic features (e.g. Keir et al., 2013).

4.1. Receiver functions observations

4.1.1. Northern profile

For the stations located on the western plateau (N001 to N005), the Pms phase is observed 6 s after the direct P-wave arrival time. Before the Pms phase, i.e. within 1.0–4.0 s after the direct P-wave arrival time, we observe a strong and coherent negative intra-crustal phase and two positive intra-crustal phases on the majority of the individual (Figs. 3 and S1) and stacked radial receiver functions (Figs. 2 and S2e). The arrival time and amplitude of the first positive phase depends on the back-azimuth (Figs. 3 and S1), and could be a P-to-S conversion at the bottom of a low velocity shallow layer or could suggest anisotropy or dipping layers. The second strong positive phase is interpreted as a conversion from a mid-crustal interface at ~20 km depth. A clear positive and coherent conversion phase (Phs) arrives behind the Moho P-to-S conversion phase (Pms) at ~9.5 s delay time (Fig. S1e), that Levin and Park (2000) associated with the Hales discontinuity and was reported by previous RFs studies beneath Nubian and Arabian continental shields (Sandvol et al., 1998; Park and Levin, 2001; Ayele et al., 2004).

The amplitudes of the transverse components are much smaller than the corresponding radial amplitudes (Fig. 2c and d). The transverse receiver functions show an intracrustal negative and positive energy that is varying over the back-azimuth, which may suggest the presence of anisotropy (Levin and Park, 1997).

As shown in Fig. 3b, at station N006 the results show a variation in the amplitude and arrival time of the Pms-converted phase on the radial RFs as well as the polarity reversal of the direct P and Pms-converted phases on the transverse RF as a function of the back-azimuth. This suggests the presence of a dipping Moho. The azimuthal RF variations of the reverberated latter phases show a complex pattern which may indicate the presence of 3-D features such as dipping interfaces and seismic anisotropy within the crust. Such complex pattern and the lack of a homogeneous earthquake distribution with back-azimuth, mean it is not possible to do a detailed crustal anisotropy analysis.

The data from the stations located within the marginal graben at the eastern end of the northern profile (N007 and N008) show a positive intra-crustal phase in the radial receiver functions at ~ 1.3–1.5 s after the direct P-wave arrival time (Figs. 2 and 3 and S1). The most prominent positive phase visible in the majority of both individual and stacked radial receiver functions (Figs. 2 and 3 and S1) arrives within a delay

time of 3.0–5.0 s after the direct P-wave arrival and is interpreted as the P-to-S conversion phase (Pms) at the Moho discontinuity. At the easternmost station (N008), we note a clear and strong negative phase arrives following the Pms phase at ~4.0 s delay time after the P-wave arrival (Fig. 2c).

4.1.2. Southern profile

The two westernmost stations (S001 and S003) on the western plateau are characterized by a clear Pms Moho conversion phase arriving with a 6.0 s delay time after the first P–wave arrival and multiples within 18–22 s delay time. A clear pre-Moho conversion phase arrives with a 2.9 s delay time after the first P-wave arrival likely originating from an intra-crustal discontinuity between the upper and lower crusts at ~20 km depth. This phase is particularly coherent and stronger in the S003 individual receiver functions and on the stacked receiver functions of the two stations (Figs. 2 and 3). The transverse RFs of the stations S001 and S003 show significant energy associated with a group of positive and negative pulses preceding the Pms Moho conversion phase. At the expected arrival time of the Pms conversion phase the transverse RFs display small positive amplitudes for the events approaching the station from easterly back-azimuths, (Fig. S2a).

The four stations (S004, S005, S006 and S007) positioned within the basin of the foothill area between the western plateau and the marginal graben are characterized by a clear Moho conversion phase (Figs. 1 and 2 and S2b). At station S004, the Pms conversion phase arrives with a delay of 5.0 s after the arrival of the direct P phase with PpPs and PsPs multiples arriving at 16.5 s and 21.0 s, respectively. At stations S005, S006 and S007, the Moho conversion phase Pms and its multiples (PpPs and PsPs) arrive at ~4.0–4.5 s, ~14.8–15.2 s and ~18.5–19.2 s delay time after the first arrival (Fig. 3, S1a and S2b). The transverse RFs show significant energy from intracrustal interfaces and at the expected arrival time of the Pms conversion phase, with the latter characterized by a polarity change for the events approaching the stations from eastern (positive) and western (negative) directions (Fig. S2b).

Stations sampling the marginal graben and Awra plain (S008, S009, S011, S012 and S013) show a clear Pms conversion phase arriving within a time window of 3.8–4.0 s and its multiples PpPs and PsPs arriving at 12.0–12.5 s and 15–16.0 s after the P-wave arrival time, respectively (Fig. 2, S1a and S2c). The transverse RFs show a significant negative and positive energy between the direct P wave arrival and the Moho converted phase characterized by reversed polarity in comparison with the radial RFs (Fig. S2c).

At the five stations (S014, FINE, S017, S018 and S020), which are located near and within the Afar rift axis, the radial receiver functions have two positive phases within 4 s after the P-wave arrival time (Figs. 2 and 3 and S1). The first low amplitude phase arrival has a delay time of 1–1.5 s with respect to the direct P-wave, and is more likely a conversion at the bottom of a low velocity shallow layer. We interpret the second strong and coherent phase arrival at a delay time of 3.5–3.8 s after the direct P-wave with corresponding multiples at 10–10.5 s and 13.5–14.5 s, as the conversion from the Moho (e.g. Fig. 2, S1a and S2d). The transverse RFs characterized by a clear negative and positive energy arrive between the onset of the P-wave and the Pms Moho conversion phase. In addition, we observe significant positive energy at the expected arrival time of the Pms Moho conversion phase for events approaching from east-southeast directions (Fig. S2d).

4.2. Crustal thickness and Vp/Vs ratio

The H–κ stacking results show a well-defined peak on the H-k plots (Figs. 4 and S2). The crustal thickness H and Vp/Vs estimated from receiver function analysis are shown on the topographic maps of Afar in Fig. 5a and Fig. 5b, respectively. The estimated crustal thickness (H) and Vp/Vs ratio using the H-κ stacking technique and associated errors from bootstrap method are shown in Fig. 6a, Fig. 6b and Table 1. We mention that the standard deviations in Table 1 are formal errors coming from

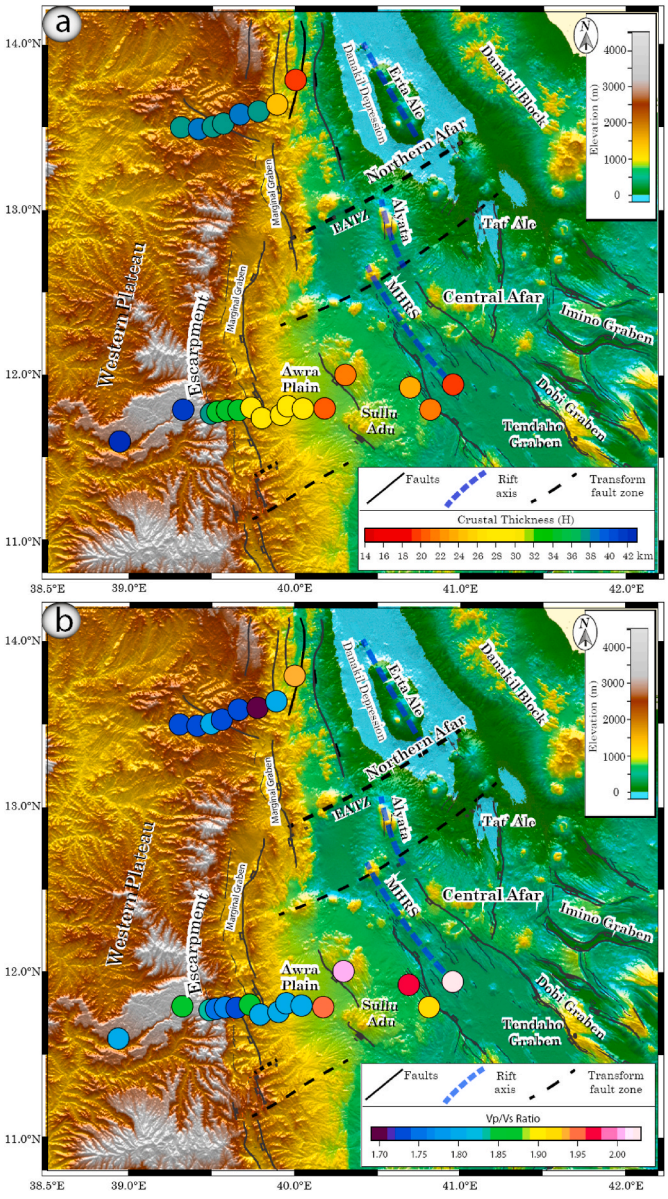

Fig. 5. Maps of crustal thicknesses (H) and Vp/Vs ratios calculated using the H-k method; a) Topographical map with the crustal thickness variations across western Afar margin and b) Topographical map with the Vp/Vs ratios across the western Afar margin. MHRS: Manda Harraro Rift Segment.

the classical bootstrap algorithm and do not include the uncertainties from the average velocity and/or vertical resolution. Therefore, the actual errors certainly will be higher recalling that any additional ±0.1 km/s uncertainty in the average crustal P-wave velocity will lead to ~ ±0.01 and ~±0.6 km uncertainties in the Vp/Vs ratio and crustal thickness, respectively.

4.2.1. Northern profile

Our crustal thickness estimates for the western plateau range from 37.2 ± 2.0 to 38.8 ± 2.1 km with an average crustal thickness of ~38.0 km. For station N006 located at the eastern edge of the western plateau, results show two peaks on the H-κ plot that correspond to discontinuities at ~28.0 km and 37.0 km, in addition to another peak corresponding to an intra-crustal interface at ~20.0 km depth (Fig. S3). Our crustal thickness estimate of ~38 km for the western plateau of the northern profile is in good agreement with the previous receiver function studies (~39.0 km; Hammond et al., 2011; Ogden et al., 2019, Fig. 7), and from

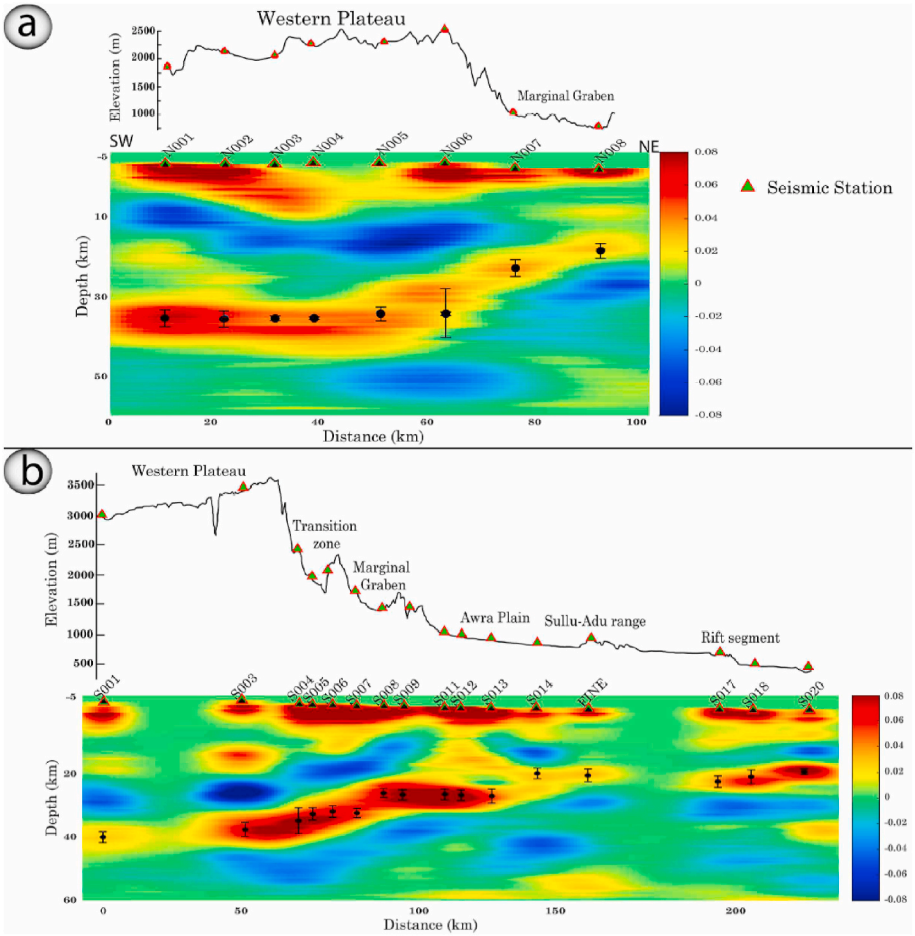

Fig. 6. Topography (vertically exaggerated) and migrated cross-sections along the two profiles. Red colour indicates velocity increase with depth, and blue colour velocity decrease with depth. Scale bar shows the amplitude of positive (red) and negative (blue) polarities of arrivals. The Moho depth estimated from H-k stacking method and corrected for the station altitude is plotted with the small circles and the vertical bars represent the errors estimated from the bootstrap method. a) Northern profile – Northern Afar and b) Southern profile – central Afar. (For interpretation of the references to colour in this figure legend, the reader is referred to the Web version of this article.)

gravity inversion (~35.0–38.0 km; Makris et al., 1991; Tiberi et al., 2005).

By comparing the Pms piercing points of N006 (H ~28.0 and 37.0 km) with the piercing points of N005 (H ~38 km) and N007 (H ~24 km) as shown in Fig. S4b, it is clear that a crustal thickness of ~37.0 km could be attributed to the plateau side to the west of this station and ~28.0 km for the foothill area to the east. We obtain 24.2 ± 1.4 km (N007) located at the foothill area and 19.6 ± 1.0 km (N008) at the eastern edge of the marginal graben (Figs. 5a and S5). Our estimated crustal thickness for N008 compare favorably with the values of 20.0 ± 2.0 km obtained by Hammond et al. (2011) for the nearby station HALE (Fig. 7).

The Vp/Vs ratio is relatively normal (1.73 ± 0.01–1.79 ± 0.02) for the stations on the western plateau (N001-N005) and for the station (N007) at the western edge of the marginal graben. Our Vp/Vs estimations are consistent with the results of ~1.71–1.77 for the stations ADYE and SMRE (Hammond et al., 2011; Ogden et al., 2019, Fig. 8). At the eastern end of the northern profile at the riftward edge of the marginal graben the N008 station shows high Vp/Vs ratio of 1.93 ± 0.04. This value compares favorably with the value of 1.98 ± 0.1 for the nearby station HALE (Hammond et al., 2011, Fig. 8).

4.2.2. Southern profile

The crustal thickness along the southern profile decreases from the W to E in three steps, such that four different zones of uniform crustal thickness and Vp/Vs ratio could be identified along the profile (Figs. 6 and S7). These zones broadly correlate with the pre-rift crust of the western plateau, the foothill area between the western plateau and the marginal graben, the stretched crust of the marginal graben and Awra plain, and finally the thinned crust within and in the vicinity of the Afar Manda-Harraro rift segment (MHRS) (Figs. 1 and S7).

We estimate an average crustal thickness of 42.0 ± 1.0 km for (S001 and S003; first zone) on the western plateau (Figs. 2 and 5a and S7). Our estimated average crustal thickness for the elevated western plateau is in good agreement with the previous P-to-S receiver functions results (38–44 km; Dugda et al., 2005; Stuart et al., 2006; Cornwell et al., 2010; Hammond et al., 2011; Kibret et al., 2019; Wang et al., 2021). It is also consistent with the crustal thickness results from joint inversion of surface waves and Pms receiver functions (~40 km; Dugda et al., 2007), with the estimates from seismic refraction profiles (40–45 km; Makris and Ginzburg, 1987; Mackenzie et al., 2005; Maguire et al., 2006) and crustal thickness from gravity inversion (~40 km; Tiberi et al., 2005).

Except for the S004 station located on/or near the steep border faults with a crustal thickness estimated to 37.2 ± 4.0 km, the crustal thickness for (S005-S007; second zone) within the foothill area is 33.8–34.2 km, with an average crustal thickness of 34.0 ± 1.2 km (Figs. 5a and S7 and Table 1). In the third zone of extended crust beneath the marginal graben and the Awra plain, five stations (S008, S009, S011, S012 and S013) with a spacing of 5–12 km were used to constrain the crustal thickness (Figs. S1 and S7). The associated crustal thickness ranges from 27.6 to 28.6 km (Table 1), with an average value of 28.0 km. Our estimates of the crustal thickness of ~28.0 ± 1.0 km for the third zone are consistent with the previous P-to-S receiver function results (~25.0–29.0 ± 1.3 km; Hammond et al., 2011).

The H-κ estimates for the crustal thickness of (S014, FINE, S017, S018 and S020; fourth zone) within and in the vicinity of the rift axis of central Afar range from 19.6 km to 23.2 km (Fig. S7, Table 1), with an average value of 21.0 ± 1.0 km. Our crustal thickness result of ~21.4 ± 0.4 at the station FINE is similar to the result obtained by Hammond et al. (2011) using data from the same station. For the other stations of

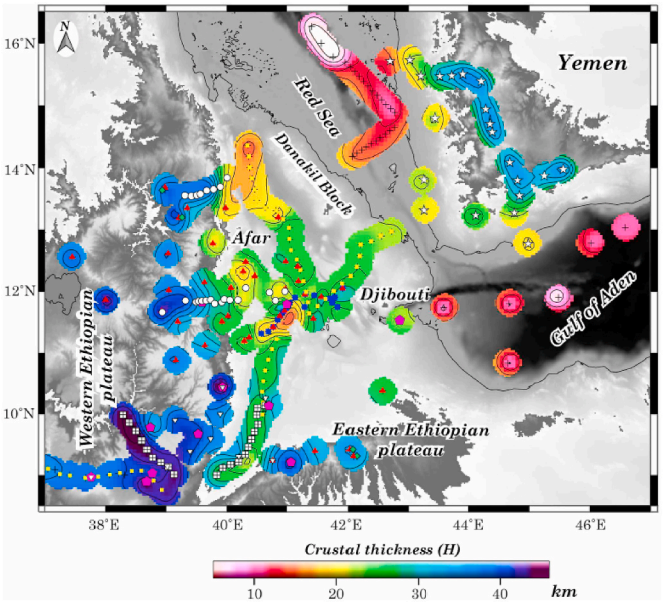

Fig. 7. Regional map showing crustal thickness (H) based on the results of the current study (white circles) and previous RF studies in Ethiopia (green diamond, Ogden et al., 2019; blue stars, Rooney et al., 2018; red triangles, Hammond et al., 2011; inverted white triangles, Stuart et al., 2006; magenta pentagon, Dugda et al., 2005), RF in Yemen (white stars, Ahmed et al., 2013). Active seismic profiles (+sign), in Afar, Ethiopian plateau and Main Ethiopian Rift (Berckhemer et al., 1975; Makris and Ginzburg, 1987: yellow square with + sign; Maguire et al., 2006: white square with + sign), in the Red Sea (Egloff et al., 1991), and the Western Gulf of Aden (Laughton and Tramontini, 1969). (For interpretation of the references to colour in this figure legend, the reader is referred to the Web version of this article.)

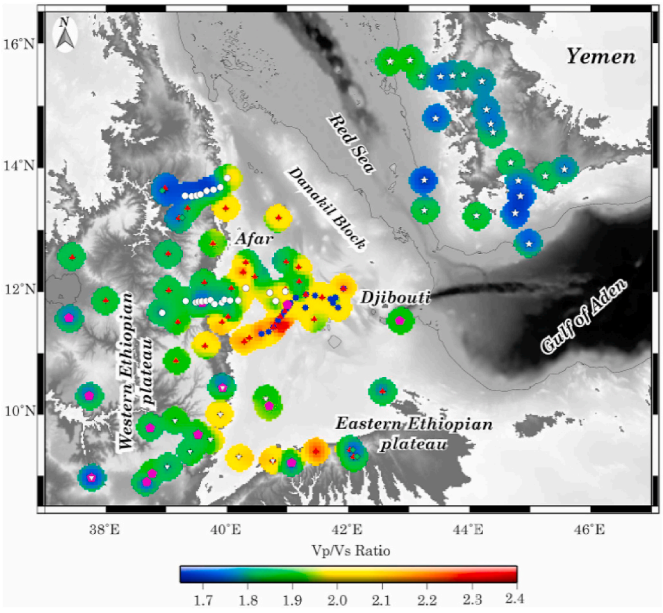

Fig. 8. Regional map showing Vp/Vs ratio based on the results of the current study (white circles) and previous RF studies in Ethiopia (green diamond, Ogden et al., 2019; blue stars, Rooney et al., 2018; red triangles, Hammond et al., 2011; inverted white triangles, Stuart et al., 2006; magenta pentagon, Dugda et al., 2005), RF in Yemen (white stars, Ahmed et al., 2013). (For interpretation of the references to colour in this figure legend, the reader is referred to the Web version of this article.)

the easternmost zone within and in the vicinity of the rift axis of central Afar our average crustal thickness value of 21.0 ± 1.0 km is in a good agreement with result obtained by Hammond et al. (2011) and Reed et al. (2014) (Fig. 7).

Our Vp/Vs ratios for the southern profile could be grouped into two main groups of the western marginal area and central rift area. Eleven stations located within the western marginal area, seven of them associated with intermediate crustal composition show elevated Vp/Vs ratios in the range from 1.79 to 1.87 and three stations located within the second zone of the foothill area, show low to normal Vp/Vs ratios in the range 1.72 ± 0.01 to 1.76 ± 0.03. Our Vp/Vs results for the stations on the western plateau and within the marginal area of central Afar (southern profile) are similar to the results from the previous receiver function studies (~1.81–1.85 ± 0.05; Hammond et al., 2011; Dugda et al., 2005, Figs. 8 and S7). Regarding the stations at the foot of the escarpment (half graben basin), our Vp/Vs values are consistent with the results obtained by Dugda et al. (2005) and Hammond et al. (2011) for the nearby station DIYA.

On the eastern end of the southern profile, data from S014, FINE, S017, S018 and S020 stations located to the west and within the MHRS show high Vp/Vs ratio of 1.94 ± 0.08, 1.99 ± 0.02, 1.95 ± 0.01, 1.91 ± 0.01 and 2.04 ± 0.02, respectively (Figs. 5b and S7). Our high Vp/Vs values above 1.9 are comparable to the results for the nearby stations obtained by Hammond et al. (2011) and slightly less than the values estimated by Reed et al. (2014) for the region to southeast of our stations (Fig. 8).

4.3. Depth migrated profiles

The velocity models used for migrated cross section are shown in Fig. S4a. Fig. 6 shows the migrated receiver functions along the northern and southern profiles. The Moho depth obtained from the H-k stacking method of Zhu and Kanamori (2000) and corrected for the station elevation is plotted with error bars from the bootstrap technique of Efron and Tibshirani (1986).

4.3.1. Northern profile

For the northern profile, the Moho interface appears as a strong positive phase (indicated by the red color, Fig. 6a) and can be easily traced. It is almost horizontal beneath the western plateau (N001-N006) at an average depth of ~36 km, and then rises in two gradual changes to a depth of ~18 km below the eastern end of the profile. The first crustal thinning (~14 km vertically over ~10 km horizontally) occurs at the edge of the plateau between N006 station located on the western plateau and N007 station located at the foot of the escarpment within the marginal graben zone. The second crustal thinning occurs within the marginal graben zone between the stations N007 and N008, (~5 km vertically over 15 km horizontally). The crust continues to thin eastward to <15 km towards Dallol within the Danakil Depression (Makris and Ginzburg, 1987; Tiberi et al., 2005; Bastow and Keir, 2011; Hammond et al., 2011).

4.3.2. Southern profile

The SW-NE-migrated image along the southern profile (Fig. 6b) shows a clear conversion from the Moho at a depth range from ~39 to 40 km at the western end to ~19–20 km beneath the eastern limit of the profile. The first locus of the crustal thinning occurs at the edge of the escarpment from 42 km beneath the western plateau to ~34 km beneath the foothills zone (8 km vertically over 20 km laterally). The second locus occurs between S007 and S008 stations located at the foothills zone and the marginal graben zone, respectively, reaching an average crustal thickness of 28 km (6 km vertically over 10 km horizontal distance). The last locus of the crustal thinning is at the western edge of the Sullu-Adu range located at the eastern half of Awra basin reaching an average crustal thickness of ~21 km beneath the MHRS at the latitude ~12°N.

5. Discussion

5.1. Crustal thicknesses and architecture

5.1.1. Western plateau

For the stations located on the western plateau, observations of the high amplitude coherent Moho converted arrivals and consistent estimated crustal thickness beneath the western plateau stations of each profile indicate that the Moho interface is mostly flat beneath the western plateau, while the intra-crustal conversions are laterally variable in amplitude and depth at some stations. A recent study of Ogden et al. (2019) shows that the reliability of the high frequency RFs is very low at the center of the flood-basalt province where the gradational Moho thickness is > 13.0 km and such reliability increases toward the outside of the flood-basalt. However, they concluded that H–κ stacking maintains reliability at low frequencies when the gradational Moho thickness is less than 13.0 km. At the southern part of the western plateau, the wide-angle reflection/refraction results at the latitude of the Main Ethiopian Rift (MER) show a ~47.0 km thick crust. This study constrained the thickness of the high-velocity layer at the bottom of the lower crust to be ~15.0 km with clear reflections from the top and bottom of this layer and an apparent velocity of 7.4 kms^{-1}. Cornwell et al. (2010), show that the high-velocity layer thins northeastward from 18.0 to 6.0 km with clear Pms conversions from the top and the bottom of the layer.

Our receiver function (calculated with both a maximum frequency of ~0.6 and ~1.2 Hz; e.g. Cassidy, 1992; Julia et al., 2005) from the station located at the eastern edge of the western plateau along the southern profile does not show double peak Pms phase (Fig. 3a, d and S2a). Instead, it shows a large amplitude intracrustal phase and Pms converted phase with a lag time of 6s, the latter consistent with the Pms phase from the bottom of the high-velocity layer of Cornwell et al. (2010), as well as a strong crustal reverberation (Fig. 3d). Our results are consistent with a recent receiver function study by Wang et al., (2021), which yielded the highest stacking amplitude values for the western plateau nearby to our stations. This indicates that the Moho beneath the stations on the western plateau is flat with a large change in seismic velocity between the crust and the mantle and does not allow us to constrain the thickness of the intruded high-velocity layer. This could also be due to a thin intruded layer (<4.0 km) below the vertical resolution owing to the wavelength of the incoming plane waves and/or to a low velocity contrast between this layer and the overlying part of the lower crust. However, if the crust-mantle transition is not a sharp boundary, our estimated crustal thickness depends on the long wavelength of the teleseismic waves we use, and more likely to select the center of the crust-mantle transition gradient (e.g. Ogden et al., 2019). In that case, we estimate the crustal thickness (include the magmatic additions) to be ~45.0–46.0 km in comparison with the average crustal thickness of ~38.0 km for the plateau beneath the northern profile (off-flood-basalt stations). In fact, the Jurassic sediments (pre-flood basalts surface) lie at an average altitude of ~2200 m (Gani et al., 2007), and the higher topography (~3700 m) of the western plateau at the latitude of the southern profile is due to the emplacement of ~1500–1800 m-thick flood-basalts deposits at the top of the Jurassic sediments. Hence, if the crust-mantle transition is a sharp boundary, then this has the implication that the western plateau is still under dynamic support process as proposed by Sembroni et al. (2016). On the other hand, if the crust-mantle is a gradational boundary of ~8.0 km thickness, the implications are that the western plateau is locally compensated with magmatic additions at the base of the lower crust as Tiberi et al. (2005) concluded from interpretation of gravity and seismic data.

Most of the western plateau stations of the northern and southern profiles show a clear intra-crustal conversion phase with a lag time of ~2.9–3.0 s from a mid-crustal discontinuity at ~20.0–21.0 km depth, likely showing the upper crust-lower crust boundary beneath the western plateau, similar to the discontinuity mentioned by Hammond et al. (2011). Toward the southern part of the western plateau at the latitude of the Main Ethiopian Rift (MER), a clear intracrustal interface is modeled by the active seismic profile. This interface separates the upper and lower crust with Vp of 6.1–6.4 kms^{-1} and 6.6–7.1 kms^{-1}, respectively (Makris and Ginzburg, 1987; Mackenzie et al., 2005; Maguire et al., 2006). A similar interface has been reported and interpreted as the Conrad discontinuity in previous receiver function studies of the eastern Red Sea conjugate margin of Yemen and southeastern Gulf of Aden margin (Ahmed et al., 2013, 2014). It was estimated at the same depth of ~21.0 km beneath the Yemen plateau covered by the Cenozoic continental flood basalts (Ahmed et al., 2013). Previous seismic refraction profiles across the Arabian shield confirm the existence of this interface between the upper crust with an average Vp of 6.3 kms^{-1} and the lower crust with an average Vp of 7.0 kms^{-1} (Mooney et al., 1985; Egloff et al., 1991). This discontinuity suggests a mafic composition for the lower crust, likely altered by magmatic intrusions or partial melt as a result of Miocene-Oligocene flood basalt and the ongoing magmatic activity (Hammond et al., 2011; Ahmed et al., 2013). Interestingly, this interface is almost imaged at the same depth of 20–21 km beneath the Arabian shield, beneath Jordan (Mooney et al., 1985; Stern and Johnson, 2010; and references therein), beneath Yemen plateau (Ahmed et al., 2013) and beneath the western plateau in this study. Although the exact physical meaning of this discontinuity is not clear, it most likely separates the slower brittle upper crust from the faster ductile lower crust (Stern and Johnson, 2010).

Our Vp/Vs values for the undeformed northern part of the western plateau with 1000–2000 m sedimentary cover are below 1.80 with an average value of ~1.74. This is lower than the global average of 1.77 and best explained by Precambrian crust of felsic to intermediate compositions (Zandt and Ammon, 1995; Christensen, 1996), which is lacking significant magmatic modification before or during the breakup (Christensen and Mooney, 1995; Thompson et al., 2010; Ogden et al., 2019).

The western plateau at the latitude of the southern profile is characterized by elevated Vp/Vs values which may indicate that the lower crust composition has been modified due to mafic intrusions associated with the Cenozoic flood basalts (Hofmann et al., 1997; Pik et al., 1999; Mackenzie et al., 2005; Cornwell et al., 2010; Hammond et al., 2011), partial melt in the lower crust (Hammond et al., 2011; Ahmed et al., 2013), or fluids circulation within the upper crust (Keir et al., 2009; Korostelev et al., 2015; Chambers et al., 2019).

5.1.2. Crustal thinning and composition across western Afar margin

5.1.2.1. Northern Afar. Our high-resolution profile of the crustal structure across the northern Afar margin into the Danakil Depression offers an opportunity to interpret the rifting evolution leading to the establishment of the current highly active divergent plate boundary. Taking into account the previous constraints on the crustal thickness near Erta'Ale rift zone and the Dallol Depression deduced by Makris and Ginzburg (1987) and Hammond et al. (2011), the variations of the Moho depth estimated in this study can be extended from the margin to the active rift axis.

The onset of the crustal extension occurs at the ~1400 m high escarpment between N006 and N007 stations, (i.e. between 39.8°E–39.9°E; Figs. 1 and S6) with ~14.0 km vertical thinning over ~10.0 km horizontal distance. The crustal thinning continues eastward in two more gradient changes before the crust reaches a thickness of ~14.0 km at the rift axis (Berckhemer et al., 1975; Makris and Ginzburg, 1987). We note that, the lateral change of the crustal thickness across the western margin of northern Afar shows comparable crustal thickness variations to that beneath Yemen, which is the eastern Red Sea conjugate margin of Ethiopia. The crustal thickness is ~35.0 km beneath the Yemen plateau, ~22.0 km for the Yemen coastal plain and a lowest value of ~14.0 km on the Yemen Red Sea coast (Ahmed et al., 2013,

Fig. 7).

Our close station spacing allows us to constrain the locus of the crustal extension more precisely than previous studies. Assuming a pre-rift crustal thickness of 38.0 km beneath the western plateau, a crustal thickness of ~19.0 km beneath the marginal graben and reaching the final thickness of ~14.0 km at the rift axis. We estimate a stretching factor β of ~2.0 for the marginal graben and β of ~2.7 for the northern Afar area between the western plateau and the rift axis. This factor obtained for northern Afar is slightly higher than the maximum value obtained for the Yemen Red Sea conjugate margin (β ~ 2.5, Ahmed et al., 2013, Fig. 8).

There is a clear eastward change of the Vp/Vs ratio from low-to-intermediate values, below the western plateau and the area at the foot of the escarpment (<1.80) to high values for the area near the eastern border faults of the marginal graben (>1.90), and reaching very high values (>2.0) at the current rift axis (e.g. Hammond et al., 2011). The high Vp/Vs ratio we found for the station N008 indicates an important change in the bulk composition of the crust due to mafic intrusions along the eastern boundary antithetic faults of the marginal graben (Illsley-Kemp et al., 2018; Zwaan et al., 2020b) or could be due to the existence of crustal fluids. The reported eastward increase in the Vp/Vs ratios toward the rift axis (Hammond et al., 2011) suggests more mafic/ultramafic material and/or may indicate a partial melting within the crust increasing with proximity of the rift axis. This is consistent with observations of recent magma intrusion related ground deformation at the axis of the Danakil Depression (e.g. Nobile et al., 2012; Pagli et al., 2012).

The structure of the northern Afar margin has been primarily controlled by a stretching phase in the early stages of continental rifting c.a ~26-20 Ma (Ukstins et al., 2002; Wolfenden et al., 2005), most likely related to the extension induced by the divergence between Arabian and Nubian plates. It should be noted that during this tectonic event the thickness of both the upper crust and lower crust decreases by a factor of two. This is evident from the depth of the mid-crustal discontinuity dropping from ~20.0 km beneath the western plateau to ~9.0–10.0 km beneath the eastern edge of the marginal graben (station N008; Figs. 6a and S2e). In the late stages of continental rifting the extension between the marginal grabens and the rift axis is accommodated by thinning of the upper crust by a factor of 2, while the lower crustal thickness remains constant. This is also evident from the mid-crustal discontinuity at ~5.0 km beneath the Danakil Depression (Makris and Ginzburg, 1987). This significant thinning of the upper crust over short length scales is consistent with geological constraints suggesting that rifting along the marginal area of northern Afar associated with upper crustal extension and dominant tectonic deformation (Bastow and Keir, 2011; Keir et al., 2013; Bastow et al., 2018). In contrary, an increase in rift magmatism associated with dike intrusions confined to the rift axis has initiated relatively recently (Quaternary) in the evolution of the rifting of northern Afar (e.g. Bastow and Keir, 2011; Nobile et al., 2012; Pagli et al., 2012).

5.1.2.2. Central Afar. Unlike the northern profile, in central Afar the number of stations along the southern profile allows us to continuously image the Moho depth and to constrain the crustal composition variations from the western plateau to the rift axis. The crustal thickness decreases eastward by ~8.0 km over ~20.0 km horizontal distance between the western plateau and the second zone located at the foot of the ~1700 m high escarpment. Then it decreases in two more steps by ~6.0 km and ~7.0 km over ~10.0 km horizontal distance from the second to the third and to the fourth zones, respectively (Fig. S7). The estimated β factors between these zones are 1.24, 1.21 and 1.30 respectively. We estimate an overall β of 2.1 for central Afar assuming an initial crustal thickness of ~42.0 km beneath the western plateau and a final crustal thickness of ~20.0 km (S020) at the eastern end of the profile. Our estimated stretching factor β for central Afar is comparable with the estimate from the previous receiver function studies (Hammond et al., 2011) but remains smaller than the β value of 3.0 and 2.7 predicted from plate reconstructions (Wolfenden et al., 2005) and from cross section balancing (Stab et al., 2016), respectively. The discrepancy between our estimated β and the predicted β is best explained by magmatic addition to the crust during extension (e.g. Mackenzie et al., 2005; Thybo and Nielsen, 2009). This implies 4.0 or 5.0 km of magmatic addition depending on the predicted β value used.

Most of the stations located within the western marginal area of central Afar (southern profile) show elevated Vp/Vs ratios which suggest intermediate to mafic composition except three stations that show low to normal Vp/Vs ratios. The latter with low to normal values are located within the foothill area and reflect that the Precambrian felsic crust has been poorly contaminated or intruded by mafic rocks. These low Vp/Vs values could also result from the emplacement of felsic volcanic strata coincidence with the onset of faulting along the central Afar margin (26-22 Ma; Wolfenden et al., 2005; Rooney et al., 2018; Ayalew et al., 2019) and/or that the crust has been intruded by granitic plutons such as along the Yemen conjugate margin (Hughes and Beydoun, 1992; Davison et al., 1994; Geoffroy et al., 1998; Ahmed et al., 2013). The slightly elevated values for the other stations that are distributed in the marginal graben and the Awra plain may indicate that the lower crust composition has been modified due to mafic intrusions associated with the Cenozoic flood basalts and/or late Miocene magmatic activity (Hofmann et al., 1997; Pik et al., 1999; Cornwell et al., 2010; Hammond et al., 2011; Rooney, 2020). It could also indicate partial melt in the lower crust (Hammond et al., 2011; Ahmed et al., 2013; Wang et al., 2021), fluids circulation within the upper crust (Keir et al., 2009; Korostelev et al., 2015; Chambers et al., 2019), or thick sedimentary deposits within the basin (Stab et al., 2016).

Finally, at the vicinity and within the MHRS, the significant increase in the Vp/Vs ratio is coincident with the thin crust (20.0 km) toward the central axis of the rift. Such high values of Vp/Vs ratio above 1.90 are very rare (except for few minerals like serpentine) and likely indicate a small amount of partial melt and/or fluids in the crust (Watanabe, 1993; Christensen, 1996; Zandt and Ammon, 1995). Hammond et al. (2011) used receiver function forward modeling for three stations located west and northwest of MHRS (to the north of our stations) to show that partial melt in the lower crust may exist beneath regions of thinner crust of central Afar. Reed et al. (2014) used the theoretical velocity-melt relationship developed by Watanabe (1993) for granitic rocks with rhyolitic melt, to estimate 4.2–11.4% melt fraction at the location of their stations located in central Afar to the southeast of our stations.

Additional observations supporting the existence of partial melt within the crust at the vicinity and within the MHRS come from imaged slow shear wave velocities within the crust and the uppermost mantle beneath the magmatic segments (Hammond et al., 2011; Stork et al., 2013; Korostelev et al., 2015; Chambers et al., 2019). Magnetotelluric results that also point to a wide conductive zones within the crust beneath MHRS interpreted as a large magma volumes that contains ~13% melt fraction (Desissa et al., 2013; Didana et al., 2014; Johnson et al., 2016) and recent series of dike intrusions at MHRS (Keir et al., 2013). Finally, Hammond (2014) invert H-κ data at three stations within and in the vicinity of MHRS for melt fraction and anisotropy and show that the melt is likely stored in the form of stacked sills within the lower crust with a maximum thickness of 2.8 km and connected by some melt inclusions in preferential vertical alignment. Hammond (2014) shows that the anisotropy, and resultant amplitude dominance of the slow shear wave in H-k stacking is a likely cause of the high Vp/Vs ratios for the average crust of the MHRS.

The crustal structure variations across the western margin of central Afar are consistent with the distinct geological and structural domains of this region. From the west, the early stretching stage of the continental rifting (c.a ~26-23 Ma; correspond to first step of the Moho interface between S003 and S004; second zone; Fig. S7) occurs below the main escarpment. This stretching phase is characterized by large offset normal

faults, distributed over a wide area (Stab et al., 2016) and accompanied with the formation of the half graben basin at the foot of the escarpment and the emplacement of felsic magmatism (Wolfenden et al., 2005). The following extension event occurs ~30.0 km eastward below the western bounding faults of the marginal graben, corresponding to the second step of the Moho interface from the second to the third zones (between S007 and S008; Fig. S7). This extension event occurs after the emplacement of many Miocene giant dykes within and in the vicinity of the marginal graben (Chorowicz et al., 1999; Stab et al., 2016; Ayalew et al., 2019; Zwaan et al., 2020b). Zwaan et al. (2020a, b) suggest that this event is related to the rotation of the Danakil block, dated from geological studies as between 16 and 7 Ma (Wolfenden et al., 2005; Zwaan et al., 2020a, 2020b). During this extension event the stretching was distributed over a wide area, most likely accompanied with the formation of antithetic normal faults and the creation of NE tilted blocks (Stab et al., 2016). A third extension event occurs below the western edge of Sullu-Adu range (between S013 and S014; Figs., 1, S7). During this event, the crust was massively intruded by the emplacement of melts within the lower crust (Hammond et al., 2011; Ayalew et al., 2019), through which the crustal composition was altered as evidenced by our high Vp/Vs ratios (Table 1; Figs., 5b, S7b).

5.2. Implications for the evolution of the rifting

We use our constraints on spatial variation in crustal thickness and Vp/Vs ratio in the 2 profiles across the Afar margin to interpret the interplay between mechanical extension (faulting and ductile stretching) and magma intrusion during rift evolution, and how these processes vary along the margin. Separated by only ~150.0 km with a major transfer zone (EATZ; Fig. 1), the two sections along the western Afar margin show strong dissimilarities in their deep structure, particularly regarding the geometry of the Moho depth across the margin. The two sections differ primarily by the amount of the stretching and the width of the extended area from the western plateau to the rift axis. The sharp decrease in the crustal thickness between the western plateau and the marginal graben during the early stages of extension ($\beta \sim 2.0$ and 1.5 for the northern and central Afar, respectively) suggests different rates of the mechanical extension. During the latter stages of extension between the marginal graben and rift axis, the differential thinning between the brittle and ductile crustal layers suggests that the two layers were decoupled and associated with mechanical extension in the brittle crust and ductile flow in the lower crust (e.g. Jolivet et al., 2015). In northern Afar, the extension during these latter stages is accommodated by the thinning of the upper crust only and distributed over a narrow extended area (~40 km). This is consistent with the high Vp/Vs ratio, the thin seismogenic layer (~5 km; Craig et al., 2011; Nobile et al., 2012) and the thin effective elastic thickness (Te ~6 km; Ebinger and Hayward, 1996; Pérez-Gussinyé et al., 2009; Ebinger et al., 2017). The stretching and thinning across the western margin of central Afar occurs on a wide distance (>100 km), accommodated by thinning of both the upper and lower crust and associated with decrease in crustal thickness by three successive steps from the stable continental western plateau to the active rift axis. Whereas the Vp/Vs ratios do not show any correlation with the crustal thickness and/or age, but well correlate to the mafic intrusions and increased melt within the crust. The crustal composition is changing from felsic at the foothill area to mafic across the marginal graben and Awra plain and ultra-mafic composition near and within the central Afar magmatic segment. These observations are consistent with a rifting history at the latitude of central Afar dominated by a discontinuous riftward migration of the extensional strain over time associated with intense magmatism (Wolfenden et al., 2005; Rooney et al., 2018; Stab et al., 2016).

6. Conclusion

We use the receiver function technique and teleseismic data recorded by a temporary broadband seismic array deployed along two profiles crossing the western margin of Afar to constrain the tectonic processes that are involved in the evolution of the rift. Our results provide constraints on the following characteristics of the crustal thickness and composition:

(1) The crustal thickness beneath the western plateau is 37–43 km, and decreases eastward to its minimum ranges from 14 to 23 km beneath the central rift axis. The decrease in the crustal thickness is more pronounced beneath the foothills and marginal grabens, but the crust also thins elsewhere in discrete steps. This is consistent with jumps in strain localization during rifting, rather than progressive strain migration. The crustal thinning of northern Afar points towards a β of 2.7, and in central Afar of 2.2. Both values are lower than a β of 3.0 predicted by plate reconstructions, with the discrepancy best explained by 2–5 km of magmatic addition to the crust. The amount of crustal thinning is higher in northern Afar, pointing towards increased plate stretching in the north.
(2) The Vp/Vs ratios suggest that the crustal composition along the western margin of Afar could be classified with unmodified crust with felsic to normal crustal composition, (western plateau next to northern Afar), altered crust due to magmatic intrusion and/or additions (western plateau and marginal area of central Afar) and highly modified crustal composition associated with the presence of partial melt at the central rift axis.
(3) There is a significant difference between the western margin characteristics of the northern Afar (Danakil Depression) in comparison with the western margin of the central Afar. In northern Afar, the crustal extension occurs over a short distance associated with significant thinning of the upper crust and dominant tectonic deformation. In central Afar, the crustal extension occurs on a wide area and characterized by multiple crustal thinning steps associated with riftward migration of the extensional deformation and intense magmatic activity.
(4) The elevated Vp/Vs ratios are generally associated with the crustal thicknesses of less than 21 km, in or near the active magmatic segments showing the role of the magmatic processes in the final stages of continental rifting.

Declaration of competing interest

The authors declare that they have no known competing financial interests or personal relationships that could have appeared to influence the work reported in this paper.

Acknowledgments

Data used in this study were collected by the AFAR17 project in Ethiopia. The instruments for the project were provided by the French National Research Infrastructure SISMOB-RESIF (http://www.resif.fr) and SEIS-UK. RESIF is supported by the French Ministry of Research and Higher Education. The facilities of SEIS-UK are supported by the Natural Environment Research Council (NERC) under agreement R8/H10/64. Funding for fieldwork (deployments, data collection and maintenance) is from Sorbonne Université, ISTEP, Institute des Sciences de la Terre de Paris. AA is supported by the Sorbonne Université (ISTeP), the University of Strasbourg (FACE program) and the PAUSE program. DK is supported by NERC grantNE/L013932/1, and MIUR grant PRIN 2017P9AT72. CP and ALR acknowledge support by the University of Pisa grant PRA_2018_19. We wish to thank the Addis-Ababa University staff for help in customs clearance and for the technical facilities, the Afar Regional Authorities and local people for their kind cooperation and their help to make the fieldwork successful. We deeply thank, Alex Nercessian, IPGP, the Centre Français d'Etudes Ethiopiennes (CFEE) in Addis-Ababa for the help and support provided by the center during the

experiment. We also deeply thank an anonymous reviewer whose comments greatly improved this manuscript.

This research has made use of the SAC (Seismic Analysis Code), TauP toolkit, GMT (General Mapping Tool) and the 1D IASP91 velocity model.

Appendix A. Supplementary data

Supplementary data to this article can be found online at https://doi.org/10.1016/j.jafrearsci.2022.104570.

References

Abdallah, A., et al., 1979. Relevance of Afar seismicity and volcanism to the mechanics of accreting plate boundaries. Nature 282, 17–23.

Ahmed, A., Tiberi, C., Leroy, S., Stuart, G.W., Keir, D., Sholan, J., Khanbari, K., Al-Ganad, I., Basuyau, C., 2013. Crustal structure of the rifted volcanic margins and uplifted plateau of Western Yemen from receiver function analysis. Geophys. J. Int. 193 (3), 1673–1690. https://doi.org/10.1093/gji/ggt072.

Ahmed, A., Leroy, S., Keir, D., Korostelev, F., Khanbari, K., Rolandone, F., Stuart, G., Obrebski, M., 2014. Crustal structure of the Gulf of aden southern margin: evidence from receiver functions on socotra island (Yemen). Tectonophysics 637, 251–267. https://doi.org/10.1016/j.tecto.2014.10.014, 337, 251-267.

Alemu, T., Abdelsalam, M.G., Dawit, E.L., Atnafu, B., Mickus, K.L., 2018. The Paleozoic e Mesozoic Mekele Sedimentary Basin in Ethiopia: an example of an exhumed IntraCONtinental sag (ICONS) basin. J. Afr. Earth Sci. 143, 40–58. https://doi.org/10.1016/j.jafrearsci.2018.03.010.

Ammon, C.J., Randall, G., Zandt, G., 1990. On the nonuniqueness of receiver function inversions. J. Geophys. Res. 95, 15 303–315 318.

Ammon, C.J., 1991. The isolation of receiver effects from teleseismic P waveforms. Bull. Seismol. Soc. Am. 81, 2504–2510.

Ayalew, D., Pik, R., Bellahsen, N., France, L., Yirgu, G., 2019. Differential fractionation of rhyolites during the course of crustal extension, Western Afar (Ethiopian rift). G-cubed 20, 571–593. https://doi.org/10.1029/2018GC007446.

Ayele, A., Stuart, G., Kendall, J., 2004. Insights into rifting from shear wave splitting and receiver functions: an example from Ethiopia. Geophys. J. Int. 157 (1), 354–362.

Ayele, A., Stuart, G., Bastow, I., Keir, D., 2007. The August 2002 earthquake sequence in north Afar: insights into the neotectonics of the Danakil microplate. J. Afr. Earth Sci. 40, 70–79.

Baker, J.A., Snee, L., Menzies, M., 1996. A brief Oligocene period of flood volcanism in Yemen: implications for the duration and rate of continental flood volcanism at the Afro-Arabian triple junction. Earth Planet Sci. Lett. 138 (1), 39–55.

Barberi, F., Varet, J., 1977. Volcanism in the Afar Depression: small-scale plate tectonic implications. Bull. Geol. Soc. Am. 88, 1251–1266.

Barberi, F., Tazieff, H., Varet, J., 1972. Volcanism in the Afar Depression: its tectonic and magmatic significance. Tectonophysics 15, 19–29. https://doi.org/10.1016/0040-1951(72)90046-7.

Barnie, T.D., Keir, D., Hamling, I., Hofmann, B., Belachew, M., Carn, S., et al., 2016. A multidisciplinary study of the final episode of the Manda Hararo dyke sequence, Ethiopia, and implications for trends in volcanism during rifting cycle. In: Vye-Brown, C. (Ed.), Geo. Soc. London, Spec. Pub. 420, 149–163. https://doi.org/10.1144/SP420.6.

Bastow, I., Keir, D., 2011. The protracted development of the continent ocean transition in Afar. Nat. Geosc. 4 (4), 248–250. https://doi.org/10.1038/NGEO01095.

Bastow, I.D., Booth, A.D., Corti, G., Keir, D., Magee, C., Jackson, C.A.-L., etal, 2018. The development of late-stage continental breakup: seismic reflection and borehole evidence from the Danakil Depression, Ethiopia. Tectonics 37, 2848–2862. https://doi.org/10.1029/2017TC004798.

Beccaluva, L., Bianchini, G., Natali, C., Siena, F., 2009. Continental flood basalts and mantle plumes: a case study of the northern Ethiopian plateau. J. Petrol. 50 (7), 1377–1403. https://doi.org/10.1093/petrology/egp024.

Berckhemer, H., Baier, B., Bartlesen, H., Behle, A., Burkhardt, H., Gebrande, H., Markris, J., Menzel, H., Miller, H., Vees, R., 1975. Deep seismic soundings of the Afar region and on the highland of Ethiopia. In: Afar Depression of Ethiopia: Proceedings of an International Symposium on the Afar Region and Related Rift Problems, Held in Bad Bergzabern, FR Germany. Schweizerbart, Stuttgart, Germany, pp. 89–107. April 1–6, 1974.

Beyene, A., Abdelsalam, M.G., 2005. Tectonics of the Afar Depression: a review and synthesis. J. Afr. Earth Sci. 41, 41–59.

Bosworth, W., Huchon, P., McClay, K., 2005. The Red Sea and Gulf of aden basins. J. Afr. Earth Sci. 43, 334–378.

Buck, W.R., 2004. Consequences of asthenospheric variability on continental rifting. In: Karner, G., Taylor, B., Driscoll, N.W., Kohlstedt, D.L. (Eds.), Rheology and Deformation of the Lithosphere at Continental Margins. Columbia University Press, New York, pp. 1–30.

Burdick, L.J., Langston, C.A., 1977. Modeling crustal structure through the use of converted phases in teleseismic body waveforms. Bull. Seismol. Soc. Am. 67, 677–692.

Cannat, M., Manatschal, G., Sauter, D., Péron-Pinvidic, G., 2009. Assessing the conditions of continental breakup at magma-poor rifted margins: what can we learn from slow spreading mid-ocean ridges? C. R. Geosci. 341, 394–405.

Cassidy, J.F., 1992. Numerical experiments in broad-band receiver function analysis. Bull. Seismol. Soc. Am. 82, 1453–1474.

Chambers, E.L., Harmon, N., Keir, D., Rychert, C.A., 2019. Using ambient noise to image the northern East African Rift. G-cubed 20, 2091–2109. https://doi.org/10.1029/2018GC008129.

Chevrot, S., van der Hilst, R.D., 2000. The Poisson ratio of the Australian crust: geological and geophysical implications. Earth Planet Sci. Lett. 183, 121–132.

Christensen, N.I., 1996. Poisson's ratio and crustal seismology. J. Geophys. Res. 101, 3139–3156.

Christensen, N.I., Mooney, W.D., 1995. Seismic velocity structure and composition of the continental crust: a global view. J. Geophys. Res. 100, 9761–9788.

Chu, R., Schmandt, B., Helmberger, D.V., 2012. Upper mantle P velocity structure beneath the Midwestern United States derived from triplicated waveforms. G-cubed 13.

Cornwell, D.G., Magurie, P.K.H., England, R.W., Stuart, G.W., 2010. Imaging detailed crustal structure and magmatic intrusion across the Ethiopian rift using a dense linear broadband array. G-cubed 11, Q0AB03. https://doi.org/10.1029/2009GC002637.

Courtillot, V., 1982. Propagating rifts and continental breakup. Tectonics 1, 239–250.

Chorowicz, J., Collet, B., Bonavia, F., Korme, T., 1999. Left-lateral strike-slip tectonics and gravity induced individualisation of wide continental blocks in the western Afar margin. Eclogae Geol. Helv. 92, 149–158. https://doi.org/10.5169/seals-168656.

Craig, T.J., Jackson, J.A., Priestley, K., McKenzie, D., 2011. Earthquake distribution patterns in Africa: their relationship to variations in lithospheric and geological structure, and their rheological implications. Geophys. J. Int. 185, 403–434. https://doi.org/10.1111/j.1365-246X.2011.04950.x.

Davison, I., et al., 1994. Geological evolution of the southeastern Red Sea rift margin, Republic of Yemen. Geol. Soc. Am. Bull. 106, 1474–1493.

Desissa, M., Johnson, N.E., Whaler, K.A., Hautot, S., Fisseha, S., Dawes, G.J.K., 2013. A mantle magma reservoir beneath an incipient mid-ocean ridge in Afar, Ethiopia. Nat. Geosci. 6, 861–865.

Didana, Y.L., Thiel, S., Heinson, G., 2014. Magnetotelluric imaging of upper crustal partial melt at Tendaho graben in Afar, Ethiopia. Geophys. Res. Lett. 41, 3089–3095. https://doi.org/10.1002/2014GL060000.

Doubre, C., Déprez, A., Masson, F., Socquet, A., Lewi, E., Grandin, R., Nercessian, A., Ulrich, P., De Chabalier, J., Saad, I., Abayazid, A., Peltzer, G., Delorme, A., Calais, E., Wright, T., 2017. Current deformation in Central Afar and triple junction kinematics deduced from GPS and InSAR measurements. Geophys. J. Int. 208, 936–953. A.

Doubre, C., Leroy, S., Keir, D., Pagli, C., RESIF, 2021. Study of the Structure of the Lithosphere from the Continental Plateau of Western Ethiopia to the Active Afar Rift (RESIF-SISMOB)[Data Set] RESIF. Reseau Sismologique et Géodésique Francais.

Dugda, M., Nyblade, A., Julià, J., Langston, C., Ammon, C., Simiyu, S., 2005. Crustal structure in Ethiopia and Kenya from receiver function analysis. J. Geophys. Res. 110, B01303 https://doi.org/10.1029/2004JB003065.

Dugda, M.T., Nyblade, A.A., 2006. New contraints on crustal structure in eastern Afar from the analysis of receiver functions and surface wave dispersion in Djibouti. In: The Afar Volcanic Province within the East African Rift System, vol. 259. Geol. Soc., London Spec. Pub., pp. 239–251

Dugda, M.T., Nyblade, A.A., Julia, J., 2007. Thin lithosphere beneath the Ethiopian plateau revealed by a joint inversion of Rayleigh wave group velocities and receiver functions. J. Geophys. Res. 112, B08305 https://doi.org/10.1029/2006JB004918.

Ebinger, C.J., Hayward, N.J., 1996. Soft plates and hot spots: views from Afar. J. Geophys. Res. Solid Earth 101, 21859–21876. https://doi.org/10.1029/96JB02118.

Eagles, G., Gloaguen, R., Ebinger, C., 2002. Kinematics of the Danakil microplate. Earth Planet Sci. Lett. 203, 607–620.

Ebinger, C., 2007. Afar. International Federation of Digital Seismograph Networks. https://doi.org/10.7914/SN/ZE_2007.

Ebinger, C.J., Keir, D., Bastow, I.D., Whaler, K., Hammond, J.O.S., Ayele, A., et al., 2017. Crustal structure of active deformation zones in Africa: implications for global crustal processes. Tectonics 36, n3298–3332. https://doi.org/10.1002/2017TC004526.

Efron, B., Tibshirani, R., 1986. The Bootstrap Method for standard errors, confidence intervals, and other measures of statistical accuracy. Stat. Sci. 1, 1–35.

Egloff, F., Rihm, R., Makris, J., Izzeldin, Y., Bobsien, M., Meier, K., Junge, P., Noman, T., Warsi, W., 1991. Contrasting structural styles of the eastern and western marginsof the southern Red Sea: the 1988 SONNE experiment. Tectonophysics 198, 329–353.

Gallacher, R., Keir, D., Harmon, N., Stuart, G., Leroy, S., Hammond, J., Kendall, J.-M., Ayele, A., Goitom, B., Ogubazghi, G., Ahmed, A., 2016. The initiation of segmented buoyancy-driven melting during continental breakup. Nat. Comms 7. https://doi.org/10.1038/ncomms13110.

Gani, N.D., Gani, M.R., Abdelsalam, M.G., 2007. Blue Nile incision on the Ethiopian Plateau: pulsed plateau growth, Pliocene uplift, and hominin evolution. GSAToday17 4.

Geoffroy, L., Huchon, P., Khanbari, K., 1998. Did Yemeni tertiary granites intrude neck zones of a stretched continental upper crust? Terra. Nova 10, 196–200.

Geoffroy, L., 2005. Volcanic passive margins. C. R. Geoscience 337, 1395–1408.

Grandin, R., Socquet, A., Binet, R., Klinger, Y., Jacques, E., de Chabalier, J.-B., Pinzuti, P., 2009. September 2005 Manda Hararo-Dabbahu rifting event, Afar (Ethiopia): constraints provided by geodetic data. J. Geophys. Res. 114 https://doi.org/10.1029/2008JB005843.

Hammond, J.O.S., Kendall, J.-M., Stuart, G., Keir, D., Ebinger, C., Ayele, A., Belachew, M., 2011. The nature of the crust beneath the Afar triple junction: evidence from receiver functions. G-cubed 12, Q12004. https://doi.org/10.1029/2011GC003738.

Hammond, J.O.S., 2014. Constraining melt geometries beneath the Afar Depression, Ethiopia from teleseismic receiver functions: the anisotropic H-κ stacking technique. G-cubed 15, 1316–1332. https://doi.org/10.1002/2013GC005186.

Hayward, N.J., Ebinger, C.J., 1996. Variations in the along-axis segmentation of the Afar rift system. Tectonics 15, 244–257.
Hofmann, C., Courtillot, V., Feraud, G., Rochette, P., Yirgu, G., Ketefo, E., Pik, R., 1997. Timing of the Ethiopian flood basalt event and implications for plume birth and global change. Nature 389, 838–841.
Hughes, G.W., Beydoun, Z.R., 1992. The Red Sea–Gulf of aden: biostratigraphy, lithostratigraphy and palaeoenvironments. J. Petrol. Geol. 15, 135–156.
Illsley-Kemp, F., Keir, D., Bull, J.M., Gernon, T.M., Ebinger, C., Ayele, A., et al., 2018. Seismicity during continental breakup in the Red Sea rift of northern Afar. J. Geophys. Res. Solid Earth 123, 2345–2362. https://doi.org/10.1002/2017JB014902.
Jolivet, L., Menant, A., Sternai, P., Rabillard, A., Arbaret, L., Augier, R., Laurent, V., Beaudoin, A., Grasemann, B., Huet, B., Labrousse, L., Le, L., 2015. The geological signature of a slab tear below the Aegean. Tectonophysics 659, 166–182. https://doi.org/10.1016/j.tecto.2015.08.004.
Johnson, N.E., Whaler, K.A., Hautot, S., Fisseha, S., Desissa, M., Dawes, G.J.K., 2016. Magma imaged magnetotellurically beneath an active and an inactive magmatic segment in Afar, Ethiopia. Geol. Soc., London, Spec Pub. 14, 150000 https://doi.org/10.1144/SP420.11.
Julia, J., Ammon, C.J., Nyblade, A.A., 2005. Evidence for mafic lower crust in Tanzania, East Africa, from joint inversion of receiver functions and Rayleigh wave dispersion velocities. Geophys. J. Int. 162, 555–569.
Justin-Visentin, E., Zanettin, B., 1974. Dike swarms, volcanism and tectonics of the Western Afar margin along the Kombolcha-Eloa traverse (Ethiopia). Bull. Volc. 38, 187–205.
Keir, D., Bastow, I., Whaler, K., Daly, E., Cornwell, D.G., Hautot, S., 2009. Lower-crustal earthquakes near the Ethiopian rift induced by magma injection. G-cubed 10, Q0AB02. https://doi.org/10.1029/2009GC002382. D. G.
Keir, D., Bastow, I.D., Pagli, C., Chambers, E.L., 2013. The development of extension and magmatism in the Red Sea rift of Afar. Tectonophysics 607, 98–114. https://doi.org/10.1016/j.tecto.
Keir, D., 2017. Afar Margin Northern Profile. International Federation of Digital seismograph Network. https://doi.org/10.7914/SN/YQ_2017.
Kennett, B.L.N., Engdahl, E.R., 1991. Traveltimes for global earthquake location and phase identification. Geophys. J. Int. 122, 429–465.
Kibret, B.A., Ayele, A., Keir, D., 2019. Crustal thickness estimates beneath four seismic stations in Ethiopia inferred from p-wave receiver function studies. J. Afr. Earth Sci. 150, 264–271. https://doi.org/10.1016/j.jafrearsci.2018.11.005.
Kieffer, B., Arndt, N., Lapierre, H., Bastien, F., Bosch, D., Pecher, A., et al., 2004. Flood and shield basalts from Ethiopia: magmas from the African superswell. J. Petrol. 45, 793–834. https://doi.org/10.1093/petrology/egg112.
Kind, R., Yuan, X., Saul, J., Nelson, D., Sobolev, S., 2002. Seismic images of crust and upper mantle beneath Tibet: evidence for Eurasian plate subduction. Science 298, 1219–1221. S.
Korostelev, F., et al., 2015. Magmatism on rift flanks: insights from ambient noise phase velocity in Afar region. Geophys. Res. Lett. 42, 2179–2188.
Krans, S., Rooney, T., Kappelman, J., Yirgu, G., Ayalew, D., 2018. From initiation to termination: a petrostratigraphic tour. Contrib. Mineral. Petrol. 173, 37.
Langston, C.A., 1977. Corvallis, Oregon, crustal and upper mantle structure from teleseismic P and S waves. Bull. Seismol. Soc. Am. 67, 713–724.
Langston, C.A., 1979. Structure under Mount Rainier, Washington, inferred from teleseismic body waves. J. Geophys. Res. 84, 4749–4762.
Laughton, A.S., Tramontini, C., 1969. Recent studies of the crustal structure of the Gulf of Aden. Tectonophysics 8, 359–375.
Lavayssiere, A., Rychert, C.A., Harmon, N., Keir, D., Hammond, J.O.S., Kendall, J.M., et al., 2018. Imaging lithospheric discontinuities beneath the northern East African Rift using S-to-P receiver functions. Geochem. Geophys., Geosyst. 19, 4048–4062. https://doi.org/10.1029/2018GC007463.
Lavier, L.L., Manatschal, G., 2006. A mechanism to thin the continental lithosphere at magma-poor margins. Nature 440, 324–328.
Le Gall, B., Leleu, S., Pik, R., Jourdan, F., Chazot, G., Ayalew, D., Yirgu, G., Cloquet, C., Chauvet, F., 2018. The Red Beds series in the Erta Ale segment, North Afar. Evidence for a 6 Ma-old post-rift basin prior to continental rupturing. Tectonophysics 747–748, 373–389.
Leroy, S., et al., 2010. Contrasted styles of rifting in the eastern Gulf of Aden: a combined wide-angle, multichannel seismic, and heat flow survey. G-cubed 11 (7), 1–14. https://doi.org/10.1029/2009GC002963.
Leroy, S., Razin, F., Autin, J., Bache, F., d'Acremont, E., Watremez, L., Robinet, J., Baurion, C., Denèle, Y., Bellahsen, N., Lucazeau, F., Rolandone, F., Rouzo, S., Serra, KielJ., Robin, C., Guillocheau, F., Tiberi, C., Basuyau, C., Beslier, M.-O., Ebinger, C., Stuart, G., Ahmed, A., Khanbari, K., AlGanad, I., de Clarens, P., Unternehr, P., Al Toubi, A., Al Lazki, A., 2012. From rifting to oceanic spreading in the Gulf of Aden: a synthesis. Arabian J. Geosci. 5 (5), 859–901. https://doi.org/10.1007/s12517-011-0475-4.
Levin, V., Park, J., 1997. Crustal anisotropy beneath the Ural mtns foredeep from teleseismic receiver functions. Geophys. Res. Lett. 24, 1283–1286.
Levin, V., Park, J., 2000. Shear zones in the proterozoic lithosphere of the arabian shield and the nature of the Hales discontinuity. Tectonophysics 323, 131–148.
Ligorria, J., Ammon, G., 1999. Iterative deconvolution and receiver functions estimation. Bull. Seismol. Soc. Am. 89, 1395–1400.
Ligorria, J.P., 2000. An Investigation of the Crust-Mantle Transition beneath North America and the Bulk Composition of the North American Crust. PhD thesis. Saint Louis University, p. 261.
Mackenzie, G.D., Thybo, H., Maguire, P.K.H., 2005. Crustal velocity structure across the Main Ethiopian Rift: results from two-dimensional wide-angle seismic modelling. Geophys. J. Int. 162, 994–1006.
Maguire, P.K.H., et al., 2006. Crustal structure of the northern Main Ethiopian Rift from the EAGLE controlled-source survey: a snapshot of incipient lithospheric break-up. In: Yirgu, G., Ebinger, C.J., Maguire, P.K.H. (Eds.), The Afar Volcanic Province within the East African Rift System, vol. 259. Geol. Soc. Spec. Publ, pp. 269–292.
Makris, J., Menzel, H., Zimmermann, J., Gouin, P., 1975. Gravity field and crustal structure of northern Ethiopia. H. In: Afar Depression of Ethiopia: Proceedings of an International Symposium on the Afar Region and Related Rift Problems, Held in Bad Bergzabern. Schweizerbart, Stuttgart, Germany, pp. 135–144. FR Germany, April 1–6, 1974.
Makris, J., Ginzburg, A., 1987. The Afar Depression: transition between continental rifting and sea-floor spreading. Tectonophysics 141, 199 (Tec).
Makris, J., Henke, C.H., Egloff, F., Akamaluk, T., 1991. The gravity field of the Red Sea and east Africa. Tectonophysics 198, 369–382.
Manighetti, I., Tapponnier, P., Gillot, P.-Y., Jacques, E., Courtillot, V., Armijo, R., King, G., 1998. Propagation of rifting along the Arabia-Somalia plate boundary: into Afar. J. Geophys. Res. 103, 4947–4974.
McKenzie, D.P., Davies, D., Molnar, P., 1972. Plate tectonics of the Red Sea and east Africa. Nature 224, 125–133.
Medynski, S., Pik, R., Burnard, P., Dumont, S., Grandin, R., Williams, A., et al., 2016. Magmatic cycles pace tectonic and morphological expression of rifting (Afar Depression, Ethiopia). Earth Planet Sci. Lett. 446, 77–88. https://doi.org/10.1016/j.epsl.2016.04.01.
Mohr, P., 1983. The Morton-Black hypothesis for the thinning of continental crust—revisited in western Afar. Tectonophysics 94 (1), 509–528.
Mohsen, A., Hofstetter, R., Bock, G., Kind, R., Weber, M., Wylegalla, K., Rümpker, G., DESERT Group, 2005. A receiver function study across the Dead Sea Transform. Geophys. J. Int. 160, 948–960.
Mooney, W.D., Gettings, M.E., Blank, H.R., Healey, J.H., 1985. Saudi Arabian seismic refraction profile: a traveltime interpretation of crustal and upper mantle structure. Tectonophysics 111, 173–246.
Nair, S.K., Gao, S.S., Liu, K.H., Silver, P.G., 2006. Southern African crustal evolution and composition: constraints from receiver function studies. J. Geophys. Res. 111 (B2), 1–17. https://doi.org/10.1029/2005JB003802.
Natali, C., Beccaluva, L., Bianchini, G., Ellam, R.M., Savo, A., Siena, F., Stuart, F.M., 2016. High-MgO lavas associated to CFB as indicators of plume-related thermochemical effects: the case of ultra-titaniferous picrite-basalt from the Northern Ethiopian-Yemeni Plateau. Gondwana Res. 34, 29–48. https://doi.org/10.1016/j.gr.2016.02.009.
Nobile, A., Pagli, C., Keir, D., Wright, T.J., Ayele, A., Ruch, J., Acocella, V., 2012. Dike-fault interaction during the 2004 Dallol intrusion at the northern edge of the Erta ale ridge (Afar, Ethiopia). Geophys. Res. Lett. 39, L19305 https://doi.org/10.1029/2012GL053152.
Nonn, C., Leroy, S., Lescanne, M., Castilla, R., 2019. Central Gulf of Aden conjugate margins (Yemen-Somalia)_ Tectono-sedimentary and magmatism evolution in hybrid-type margins. Mar. Petrol. Geol. 105, 100–123. https://doi.org/10.1016/j.marpetgeo.2018.11.053.
Ogden, C.S., Bastow, I.D., Gilligan, A., Rondenay, S., 2019. A reappraisal of the H–κ stacking technique: implications for global crustal structure. Geophys. J. Int. 219, 1491–1513. https://doi.org/10.1093/gji/ggz364.
Pagli, C., Wright, T.J., Ebinger, C.J., Yun, S.H., Cann, J.R., Barnie, T., Ayele, A., 2012. Shallow axial magma chamber at the slow-spreading Erta Ale Ridge. Nat. Geosci. 5 (4), 284–288.
Park, J., Levin, V., 2001. Receiver functions from regional P waves. Geophys. J. Int. 147, 1–11.
Pérez-Gussinyé, M., Metois, M., Fernandez, M., Verges, J., Lowry, A.R., 2009. Effective elastic thickness of Africa and its relationship to other prozie for lithospheric structure and surface tectonics. Earth Planet Sci. Lett. 287 (1–2), 152–167. https://doi.org/10.1016/j.epsl.2009.08.004.
Pik, R., Deniel, C., Coulon, C., Yirgu, G., Hofmann, C., Ayalew, D., 1998. The northwestern Ethiopian Plateau flood basalts: classification and spatial distribution of magma types. J. Volcanol. Geoth. Res. 81, 91–111.
Pik, R., Deniel, C., Coulon, C., Yirgu, G., Marty, B., 1999. Isotopic and trace element signatures of Ethiopian flood basalts; evidence for plume lithosphere interactions. Geochem. Cosmochim. Acta 63 (15), 2263–2279. https://doi.org/10.1016/S0016-7037 (99)00141-6.
Pik, R., 2011. East-Africa on the rise. Nat. Geosci. 4, 660–661.
Phinney, R.A., 1964. Structure of Earths crust from spectral behavior of long-period body waves. J. Geophys. Res. 69, 2997–3017.
Reed, C.A., Almadani, S., Gao, S.S., Elsheikh, A.A., Cherie, S., Abdelsalam, M.G., Thurmond, A.K., Liu, K.H., 2014. Receiver function constraints on crustal seismic velocities and partial melting beneath the Red Sea Rift and adjacent regions, Afar Depression. J. Geophys. Res. Solid Earth 119, 2138–2152. https://doi.org/10.1002/2013JB010719.
Rooney, T.O., 2017. The Cenozoic magmatism of East-Africa: Part I—flood basalts and pulsed magmatism. Lithos 286, 264–301.
Rooney, T.O., Krans, S.R., Mège, D., Arnaud, N., Korme, T., Kappelman, J., Yirgu, G., 2018. Constraining the magmatic plumbing system in a zonedcontinental flood basalt province. Geochem., Geophys., Geosyst. 19, 3917–3944. https://doi.org/10.1029/2018GC007724.
Rooney, T.O., 2020. The Cenozoic Magmatism of East Africa: Part IV – the Terminal Stages of Rifting Preserved in the Northern East African Rift System: Lithos, 108381. https://doi.org/10.1016/j.lithos.2020.105381.
Rychert, C.A., Hammond, J.O.S., Harmon, N., Michael Kendall, J., Keir, D., Ebinger, C., Bastow, I.D., Ayele, A., Belachew, M., Stuart, G., 2012. Volcanism in the Afar Rift sustained by decompression melting with minimal plume influence. Nat. Geosci. 5 (6), 406–409.

Salmon, M.L., Stern, T.A., Savage, M.K., 2011. A major step in the continental Moho and its geodynamic consequences: the Taranaki–Ruapehu line, New Zealand. Geophys. J. Int. 186, 32–44. https://doi.org/10.1111/j.1365-246X.2011.05035.x.

Sandvol, E., Seber, D., Calvert, A., Barazangi, M., 1998. Grid search modeling of receiver functions: implications for crustal structure in the Middle East and North Africa. J. Geophys. Res. 103 (26), 899– 26,917.

Sembroni, A., Faccenna, C., Becker, T.W., Molin, P., Abebe, B., 2016. Longterm, deep-mantle support of the Ethiopia-Yemen Plateau. Tectonics 35, 469–488. https://doi.org/10.1002/2015TC004000.

Smittarello, D., Grandin, R., De Chabalier, J.-B., Doubre, C., Déprez, A., Masson, F., Socquet, A., Saad, A., 2016. Transient deformation in the Asal-Ghoubbet Rift (Djibouti) since the 1978 diking event: is deformation controlled by magma supply rates? J. Geophys. Res. 121 https://doi.org/10.1002/2016JB013069.

Stab, M., Bellahsen, N., Pik, R., Quidelleur, X., Ayalew, D., Leroy, S., 2016. Modes of rifting in magma-rich settings: tectono-magmatic evolution of Central Afar. Tectonics 35, 2–38. https://doi.org/10.1002/2015TC003893.

Stern, R.J., Johnson, P., 2010. Continental lithosphere of the Arabian Plate: a geologic, petrologic, and geophysical synthesis. Earth Sci. Rev. 101, 29–67.

Stork, A., Stuart, G.W., Henderson, C.M., Keir, D., Hammond, J.O.S., 2013. Uppermost mantle (Pn) velocity model for the Afar region, Ethiopia: an insight into rifting processes. Geophys. J. Int. 193, 321–328.

Stuart, G.W., Bastow, I.D., Ebinger, C.J., 2006. Crustal structure of the northern Main Ethiopian Rift from receiver function studies. In: Yirgu, G., Ebinger, C.J., Maguire, P. K.H., Soc, Geol (Eds.), The Afar Volcanic Province within the East African Rift System, vol. 259. Spec Pub, London, pp. 253–267.

Tiberi, C., Ebinger, C., Ballu, V., Stuart, G., Oluma, B., 2005. In- verse models of gravity data from the Red Sea-Aden-East African rifts triple junction zone, Geophys. J. Intell. 163, 775–787. https://doi.org/10.1111/j.1365-246X.2005.02736.x.

Tiberi, C., Leroy, S., d'Acremont, E., Bellahsen, N., Ebinger, C., Al-Lazki, A., Pointu, A., 2007. Crustal geometry of the northeastern Gulf of Aden passive margin: localization of the deformation inferred from receiver function analysis. Geophys. J. Int. 168, 1247–1260.

Tesfaye, S., Harding, D., Kusky, T., 2003. Early continental breakup boundary and migration of the Afar triple junction, Ethiopia. Geol. Soc. Am. Bull. 115 (9), 1053–1067. https://doi.org/10.1130/B25149.1.

Thompson, D.A., Bastow, I.D., Helffrich, G., Kendall, J.M., Wookey, J., Snyder, D.B., Eaton, D.W., 2010. Precambrian crustal evolution: seismic constraints from the Canadian shield. Earth Planet Sci. Lett. 297, 655-–666. https://doi.org/10.1016/j.epsl.2010.07.021.

Thybo, H., Nielsen, C.A., 2009. Magma-compensated crustal thinning in continental rift zones. Nature 457, 873–876. https://doi.org/10.1038/nature07688.

Ukstins, I.A., Renne, P.R., Wolfenden, E., Baker, J., Ayalew, D., Menzies, M., 2002. Matching conjugate volcanic rifted margns: 40 Ar/39 Ar chrono-stratigraphy of pre- and syn-rift bimodal flood volcanism in Ethiopia and Yemen. Earth Planet Sci. Lett. 198, 289–306.

Varet, J., 1975. Carte géologique de l'Afar central et méridional. CNR- CNRS, 1/500 000 Géotechni.

Wang, T., Gao, S.S., Yang, Q., Kelly, H., 2021. Crustal structure beneath the Ethiopian Plateau and adjacent areas from receiver functions: implications for partial melting and magmatic underplating. Tectonophysics 809 (C), 228857. https://doi.org/10.1016/j.tecto.2021.228857, 2021.

Watanabe, T., 1993. Effects of water and melt on seismic velocities and their application to characterization of seismic reflectors. Geophys. Res. Lett. 20, 2933–2936.

Wolfenden, E., Ebinger, C., Yirgu, G., Deino, A., Ayalew, D., 2004. Evolution of the northern Main Ethiopian rift: birth of a triple junction. Earth Planet Sci. Lett. 224, 213–228. https://doi.org/10.1016/j.epsl.2004.04.022.

Wolfenden, E., Ebinger, C., Yirgu, G., Renne, P.R., Kelly, S.P., 2005. Evolution of a volcanic rifted margin: southern Red Sea, Ethiopia. Geol. Soc. Am. Bull. 117, 846–864.

Wright, T.J., Ebinger, C., Biggs, J., Ayele, A., Yirgu, G., Keir, D., Stork, A., 2006. Magma-maintained rift segmentation at continental rupture in the 2005 Afar dyking episode. Nature 442, 291–294. https://doi.org/10.1038/nature04978.

Zandt, G., Ammon, C.J., 1995. Continental crust composition constrained by measurement of crustal Poisson's ratio. Nature 374, 152–154.

Zhu, L., 2000. Crustal structure across the san andreas fault, southern California from teleseismic converted waves, earth planet. Sci. Lett. 179, 183–190.

Zhu, L., Kanamori, H., 2000. Moho depth variation in Southern California from teleseimic receiver function. J. Geophys. Res. 105, 2969–2980.

Zwaan, F., Corti, G., Keir, D., Sani, F., 2020a. A review of tectonic models for the rifted margin of Afar: implications for continental break-up and passive margin formation. J. Afr. Earth Sci. 164, 103649 https://doi.org/10.1016/j.jafrearsci.2019.103649.

Zwaan, F., Corti, G., Sani, F., Keir, D., Muluneh, A.A., Illsley-Kemp, F., Papini, M., 2020b. Structural analysis of the western Afar margin, east Africa: evidence for multiphase rotational rifting. Tectonics 39, e2019TC006043. https://doi.org/10.1029/2019TC006043.